6

Nanoscale Effects of Friction, Adhesion and Electrical Conduction in AFM Experiments

Marius Enachescu
*University POLITEHNICA of Bucharest**
Romania

1. Introduction

Friction and adhesion are two so related phenomena of the contact formed by two bodies. And due to the presence of friction and adhesion very often we have wear, i.e., third body presence generated by friction and adhesion. Likely, friction is one of the oldest phenomena in the history of humankind and of natural science, e.g., physics. Friction was the origin of first fire lit by human in early Stone Age, and of the many events Egyptians had faced while pulling huge blocks of stone needed for their pyramids. In fact, Egyptians were basically the first tribologists in history, even if the term tribology defined as "science and technology of interacting surfaces in relative motion", was suggested only in 1966 by Peter Jost.

Humanity needed to enter into Renaissance period in order to have Leonardo da Vinci (1452-1519) (Dowson, 1979) to introduce the first modern concepts of friction. Da Vinci came to two important conclusions:

1. "*Friction produces double the amount of effort if the weight be doubled.*"
2. "*The friction made by the same weight will be of equal resistance at the beginning of the movement, although the contact may be of different breadths or lengths.*"

In other words, these are today the two fundamental laws of friction, the friction force is proportional to the load (normal force), and independent of the apparent area of contact between the sliding body and the surface.

Two centuries later, Amonton (1663-1705) rediscovered and extended da Vinci's observations. Amonton confirmed these observations with further experiments, from which came Amonton's Law of Friction: $F_f = \mu L$, which states that the friction force F_f is proportional to the applied load L. Thus, today the two fundamental laws of friction are called ''da Vinci-Amonton's laws''.

It took nearly an extra century, 1785, for the experiments of Coulomb (1736-1806) to distinguish between friction during sticking and sliding. He observed that the coefficient of kinetic friction was generally smaller than the coefficient of static friction. He also observed that μ was generally independent of sliding velocity. Investigating the origins of friction, Coulomb suggested that roughness (asperities) on the micrometer scale is responsible for the occurrence of friction, as depicted in Fig 1. However, there was experimental evidence against his hypothesis: highly polished surfaces did not exhibit low, but high friction.

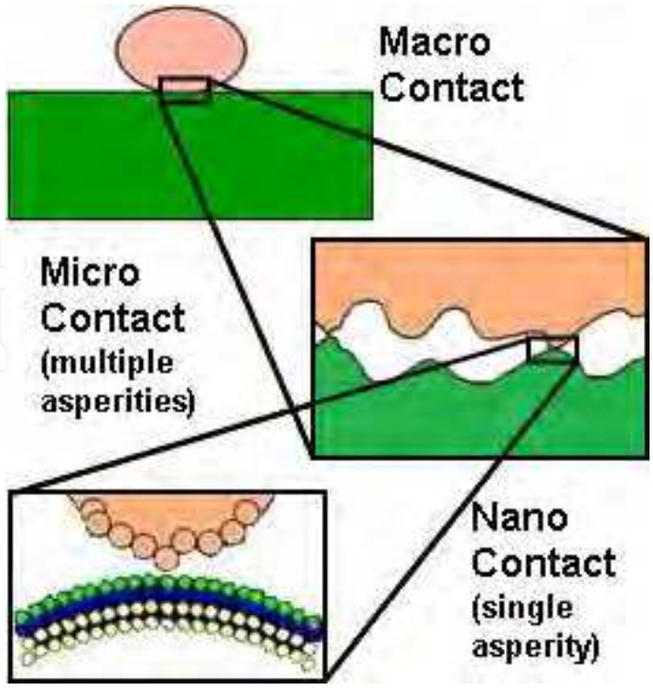

Fig. 1. A macroscopic contact that appears conforming and continuous is usually composed of multiple contact points between many microasperities. The frictional behavior of such a contact follows Amonton's Law. The friction law for a microscopic contact, a single asperity contact, is not known. A scanning probe instrument provides a well-defined single asperity contact (the tip) where interaction forces can be precisely measured with nanometer/atomic resolution. At this scale, macroscopic physical laws no longer apply. For example, the friction force (*Ff*) is no longer linearly proportional to the applied load (*L*).

An alternative explanation was given by Desaguliers, who suggested that molecular adhesion might be the relevant phenomenon. However, molecular adhesion was known to be proportional to contact area, whereas friction was found to be independent of contact area.

It is astonishing that wear phenomena, despite their obvious significance, were studied quite late. The reason for this delay may lie in the fact that the leading cause of wear is through the interactions of micro-contacts, which became an object of tribological research only after the work of Bowden and Tabor. It took about two centuries beyond Coulomb's work until this controversy was solved. Around 1950, Bowden and Tabor performed systematic, tribological experiments which showed that the contact of a macroscopic body is formed by a number of small asperities (Fig. 1). Thus, another contact area, the real area of contact had to be introduced. This new concept was extremely successful and is the basics of most present tribological studies. Essentially, the Bowden-Tabor model states that friction is proportional to the real area of contact.

From this point of view, Desaguliers was right to assume that adhesion, which is also proportional to the contact area, is more related to friction than roughness. Therefore, the model is also called Bowden-Tabor adhesion model. In first approximation, the real area of contact does not depend on the apparent contact area. By increasing the load, the number of contacting asperities also increases with load.

The Bowden-Tabor adhesion model explains the da Vinci-Amonton's laws of the macroscopic world. However, a basic understanding of friction is still lacking and many questions remain unanswered such as: i) What are the microscopic mechanisms of friction? ii) How is energy dissipated? iii) How do lubricants (third body presence) affect the shear properties? iv) Can the friction be calculated from molecular interaction potentials in a quantitative way?

During the last two decades, the field of tribology at the atomic and nanometer scale became of interest to a bigger scientific community. These problems are beginning to be addressed by relative recent development of several experimental techniques (Krim, 1996). Instruments such as the surface forces apparatus (SFA) (Israelachvili, 1972) (Israelachvili et al., 1990), the quartz-crystal microbalance (QCM) (Krim et al., 1990) (Watts et al., 1990) (Krim et al., 1991), the atomic force microscope (AFM) (Mate et al., 1987) (Binnig et al., 1986a) and others are extending tribological investigations to atomic length and time scales. Furthermore, advances in computational power and theoretical techniques are now making sophisticated atomistic models and simulations feasible (Harrison & Brenner, 1995). Nanotribology, is the emerging field that attempts to use these techniques to establish an atomic- and nano-scale understanding of interactions between contacting surfaces in relative motion (Carpick et al., 1998a; Enachescu et al., 1998, 1999a, 1999b, 1999c, 2004; Park et al., 2005a; Carpick & Salmeron, 1997; Grierson &. Carpick, 2007; Szlufarska et al., 2008).

Nanotribology, and particularly AFM experiments, focusing on the fundamentals and basic understanding of friction, adhesion, and wear, is trying to do this in terms of chemical bonding and of the elementary processes that are involved in the excitation and dissipation of energy modes.

In AFM experiments, besides the obvious friction and wear obvious experiments, adhesion measurements are easily performed via so called pull-off experiments. A basic pull-off experiment is described in Fig. 2 below.

Regarding the excitation and dissipation of energy modes during tribological experiments, several mechanisms have been investigated and proposed. One is related to coupling to the substrate (and tip) electron density that causes a drag force, similar to that causing an increase of electrical resistance by the presence of surfaces in thin films (Daly & Krim, 1996; Sokoloff, 1995; Persson & Volokitin, 1995; Persson & Nitzan, 1996). Another is related to excitation of surface phonon modes in atomic stick-slip events. Delocalization of the excited phonons by coupling to other phonon modes through nonharmonic effects and transport of the energy away from the excited volume leads to efficient energy dissipation (Sokoloff, 1993; Carpick & Salmeron, 1997). At high applied forces, an important event is the wear process leading to rupture of many atomic bonds, the creation of point defects near the surface, displacement and creation of dislocations and debris particles.

Another level of our understanding focus, and where AFM experiments may decisively contribute, includes questions such as the nature of relative motion between the two contacting bodies: is it continuous (smooth sliding) or discontinuous (stick-slip, e.g., atomic stick-slip)? How does friction depend upon the actual area of contact between two bodies? Are friction and adhesion related, and how? What is the behavior of lubricant molecules, including third bodies, at an interface? How are they compressed and displaced during loading and shear? How does their behavior depend upon their molecular structure and chemical identity? It is our intent to partially address some of these questions in the work presented here.

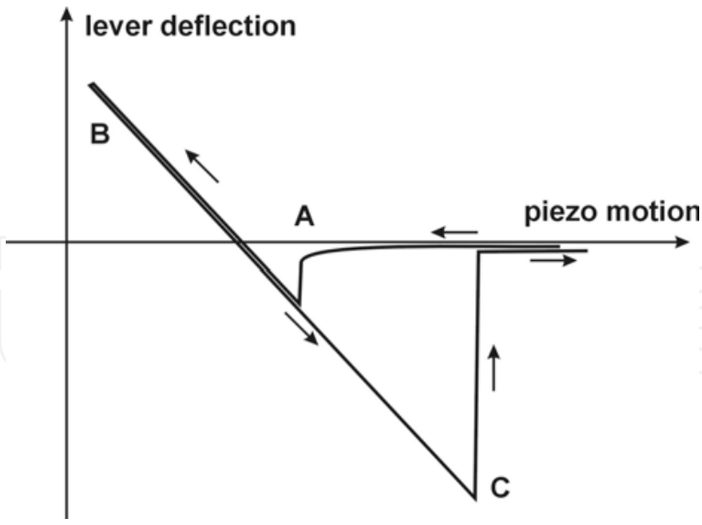

Fig. 2. A typical pull-off, or force vs. displacement curve during an approach-retract experiment. The AFM lever deflection is recorded while tip and sample are brought into contact and separated again. As long as tip and sample are separated, the free lever is not deflected. When tip and sample are brought into close proximity (A) the lever "feels" an increasingly attractive force, caused by long range electrostatic or van der Waals forces, and is bent down towards the sample. When the force gradient exceeds the spring constant of the lever, an instability, the so called "jump-to-contact", occurs, and the tip abruptly contacts the surface. Upon further approach, the lever experiences a repulsive force and is bent upwards (B), for small deflections following Hook's law. Upon reversal of the piezo motion the deflection signal follows the previous path. But adhesive forces will keep the tip in contact with the sample until the elastic force of the lever exceeds the adhesion and the lever snaps out of contact (C).

As mentioned, friction and adhesion are related phenomena of the contact formed by two bodies. And due to the presence of friction and adhesion very often we have wear, i.e., third body presence generated by friction and adhesion. Also, the interface created under friction and adhesion plays a crucial role in the local electrical conductivity between the two bodies, besides the bodies' intrinsic conductivity properties. All of these, friction, adhesion, third body presence (wear) and local conductivity at nanometer scale are the goal of this work, that is trying to bring extra light in the emerging nanotribology field.

2. Atomic- and nano-scale friction experiments on a special interface

The nanotribological properties of a hydrogen-terminated diamond(111)/tungsten-carbide interface have been studied using ultra-high vacuum atomic force microscopy. Both friction and local contact conductance were measured as a function of applied load. The contact conductance experiments provide a direct and independent way of determining the contact area between the conductive tungsten-carbide AFM-tip and the doped diamond sample. It was demonstrated that the friction force is directly proportional to the real area of contact at the nanometer-scale. Furthermore, the relation between the contact area and load for this extremely hard heterocontact is found to be in excellent agreement with the Derjaguin-Müller-Toporov continuum mechanics model.

According to the classical law of friction, the friction force between two bodies in motion is proportional to the applied load and independent of the apparent area of contact (Dowson, 1998). However, a macroscopic contact between two apparently flat solid surfaces consists in practice of a large number of micro-contacts between the asperities that are present on both contacting surfaces (Fig. 1). The classical law of friction, which cannot be understood or deduced from first principles, is the result of many complex phenomena at the interface, in particular the specific interactions between contacting asperities, and the corresponding deformations of these asperities (Greenwood & Williamson, 1966). Although macroscopic tribological research can provide important empirical information about the frictional behavior of materials, it cannot explain friction at a fundamental level. Only detailed studies of friction at a single-asperity contact, under well-defined conditions and with nanometer-scale or even atomic-scale resolution, can result in an understanding of friction at a fundamental level. Some ultra-high vacuum atomic force microscopy (UHV-AFM) experiments indicate that friction is proportional to the contact area for a nanometer-sized single-asperity contact (Carpick et al., 1996a, 1998a; Enachescu et al., 1998; Lantz et al., 1997a, 1997b). In some of these studies, the contact area was not directly measured but instead derived from continuum mechanics models, although, as discussed further below, it is generally not clear *a priori* which model is valid for a specific combination of materials. As well, most of these experiments were performed on layered materials, where it is unclear whether continuum mechanics models can be used quantitatively. Nevertheless, the continuum mechanics models generally provided convincing fits to the data. Carpick *et al.* (Carpick et al., 1996a) performed experiments on muscovite mica and found that friction was proportional to the contact area as described by the Johnson-Kendall-Roberts (JKR) model (Johnson et al., 1971). Experiments by Lantz *et al.* (Lantz et al., 1997a, 1997b) on $NbSe_2$ and graphite resulted in a relation between friction and contact area as described by the Maugis-Dugdale (MD) model (Maugis, 1992; Johnson, 1997). Only one observation of the Derjaguin-Müller-Toporov (DMT) model (Derjaguin et al., 1975; Müller et al., 1983) has been reported so far by Enachescu *et al.* (Enachescu et al., 1998). The experiments were conducted with an extremely hard heterocontact, involving stiff materials with low adhesive forces, *i.e.* a tungsten-carbide AFM-tip in contact with a hydrogen-terminated diamond(111) sample. Both diamond and tungsten-carbide are extremely stiff, non-layered materials. Furthermore, hydrogen passivates the diamond surface while carbides are generally quite inert.

In this study, we discuss the results of a nanotribological study of a hydrogen-terminated diamond(111)/tungsten-carbide single asperity interface using UHV-AFM. Since the diamond sample is slightly boron-doped and the tungsten-carbide tip is conductive, we are able to measure the local contact conductance as a function of applied load. These experiments provide an independent way of determining the contact area, which can be directly compared to the corresponding friction force. Diamond and diamond-like films are important coating materials used in a wide variety of tools, hard disks, micro-machines, and aerospace applications. For micro-machine and hard disk applications in particular, the nanotribological properties are of great importance (Seki et al., 1987). Similarly, tungsten-carbide plays an important role in several types of hard coatings (Schwartz, 1990).

2.1 Background

The AFM results (Carpick et al., 1996a, 1998a; Enachescu et al., 1998; Lantz et al., 1997a, 1997b) and surface forces apparatus (Homola et al., 1989) experiments indicate that the

friction force F_f varies with the applied load L in proportion to the tip-sample contact area A. Thus, $F_f = \tau A$ where τ is the shear strength, a fundamental interfacial property. In most cases, the relation between A and L is deduced from elastic continuum mechanics models, assuming a sphere (tip) in contact with a flat plane (sample) (Johnson, 1987). However, the correct relation between A and L not only depends on the exact geometry but also upon the strength of the adhesive forces compared to the elastic deformations (Maugis, 1992; Müller et al., 1980; Tabor, 1977; Greenwood, 1997; Johnson, 1996).

The JKR and DMT models mentioned above have been deduced for two extreme cases, namely for compliant materials with strong, short-range adhesive forces and for stiff materials with small, long-range adhesive forces, respectively. The empirical nondimensional parameter $\mu = \left(R\gamma^2 / E^{*2} z_0^3 \right)^{1/3}$ can be used to determine which of the two continuum mechanics models is most appropriate (Tabor, 1977; Johnson, 1996). In this expression, R is the sphere radius, γ is the work per unit area required to separate tip and surface from contact to infinity, and E^* is a combined elastic modulus, given by the equation $E^* = ((1-\nu_1^2)/E_1 + (1-\nu_2^2)/E_2)^{-1}$, where E_1 and E_2 are the Young's moduli, and ν_1 and ν_2 are the Poisson's ratios of the sphere and plane, respectively. Finally, z_0 represents the equilibrium spacing for the interaction potential of the surfaces. If $\mu > 5$, the JKR theory should be valid, while for $\mu < 0.1$, the DMT theory should describe the relation between A and L (Tabor, 1977; Johnson, 1996; Greenwood, 1997). Neither the JKR nor the DMT limit is appropriate for the intermediate cases ($0.1 < \mu < 5$). As discussed by Greenwood (Greenwood, 1997), it is difficult to calculate the exact area of contact for the continuum problem. Greenwood obtained a numerical solution using a Lennard-Jones potential and defined the contact edge as the point of maximum adhesive stress. Greenwood's solution closely resembles the Maugis-Dugdale model. In both cases, the variation of contact area with load then appears very close to the *shape* of the JKR curve for values of $\mu > 0.5$. However, the JKR equation does not correctly predict the *actual* contact area, pull-off force, and thus the adhesion energy, unless $\mu > 5$. Therefore, while a measurement of contact area versus load may resemble a JKR curve, quantitative analysis would be uncertain, as it would highly depend on a specific model for the tip-sample interaction potential.

In the case of the DMT model ($\mu < 0.1$), the contact area A varies with the applied load L in a simple fashion: $A = \pi \frac{R^{2/3}}{K^{2/3}} \left(L + 2\pi\gamma R \right)^{2/3}$, where K=(4/3)E*. The pull-off force or critical load L_c is given by $L_c = -2\pi\gamma R$. The value of L_c can be obtained from AFM approach/retract displacements of the cantilever and sample, by measuring the (negative) normal force required to separate tip and sample. We note that the contact area goes to zero at pull-off, in contrast to the JKR model.

The contact radius in AFM experiments is generally in the nanometer-range and, consequently, much smaller than the electronic mean free path. In this limit, the contact conductance becomes directly proportional to the contact area, as described by Sharvin's equation for metallic contacts (Jansen et al., 1980): $G = 3\pi a^2/4\rho l$, where ρ is the resistivity, l is the mean free path of the conduction electrons, and a is the radius of the contact. We stress that this equation is only valid for nanometer-sized contacts, where $l >> a$. The linear relationship between the contact conductance and contact area is true whether the junction

is Ohmic, semiconductor-like, *etc.* For instance, in the case of a metal/semiconductor contact (Sze, 1981), which matches our tip-sample interface, the current is directly proportional to the area of contact, considering a constant metal/semiconductor barrier height and a constant temperature during the experiments. We do not expect to observe the current to change step-wise with load, *i.e.,* the well-known phenomena of quantized conductance occurring at contacts consisting of only a few atoms (Rubio et al., 1996), since in our experiments the contact area contains many atoms.

2.2 Experimental

The experiments were performed in an UHV chamber (base pressure 7 x 10^{-11} Torr), since even in moderately evacuated chambers the residual oxygen and water vapor may combine with the sliding action to catalyze a phase change on diamond (Gardos, 1994). The UHV-chamber is equipped with a home-built AFM (Dai et al., 1995), low-energy electron diffraction (LEED), and Auger electron spectroscopy (AES). The sample is an artificial type IIb diamond(111) single-crystal, which is terminated with hydrogen and slightly boron-doped. The cleaning procedure used, as well as the single-crystal quality, are described in more detail by van den Oetelaar *et al.* (van den Oetelaar & Flipse, 1997). Fig 3 shows the LEED pattern taken after the cleaning procedure. This clear (1x1) LEED pattern supports the fact that we have a hydrogen-terminated diamond(111)-(1x1) surface.

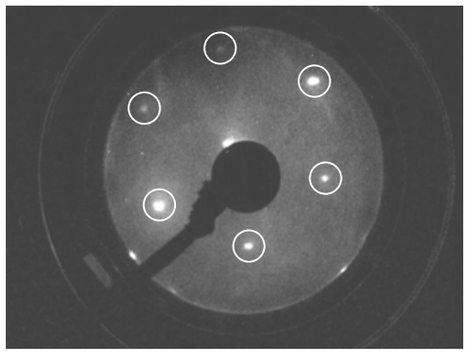

Fig. 3. Our cleaning procedure gave rise to a clear hydrogen-terminated diamond(111)-(1x1) surface, as shown in this LEED pattern.

Triangular silicon cantilevers with integrated tips, coated with approximately 20 nm tungsten-carbide, were used for all measurements. The tips were characterized by scanning electron microscopy (SEM) and AES. Two types of cantilevers were used, with a spring constant of 88 N/m and 0.23 N/m, respectively. The former cantilever was used for conductance measurements while the latter one was used for friction measurements. The tips were cleaned in UHV immediately prior to the measurements, by applying short voltage pulses and/or by rubbing them on the surface. Normal cantilever force constants were taken from the manufacturer, and the normal/lateral force ratio was calculated using the method described by Ogletree *et al.* (Ogletree et al., 1996). The absolute accuracy of the forces measured is limited due to significant uncertainty in the material properties of the cantilever and approximations used in the force constant calculations. However, relative changes in friction could be accurately determined by using the same cantilever and tip during a series of measurements. A flexible I-V converter, allowing current measurements spanning the range from pA to mA, was designed and built.

Friction versus load data were acquired by scanning the AFM-tip repeatedly back and forth over the same line on the surface, while linearly increasing or decreasing the externally applied load. The value of the friction force at a given load is half of the difference between the signals while scanning from left to right, and right to left, respectively (Carpick et al., 1996a; Hu et al., 1995).

2.3 Results and discussions

All of the results presented in this work were obtained on a hydrogen-terminated diamond(111) sample, consisting of atomically smooth and well-ordered islands of 150 - 250 Å in diameter (Enachescu et al., 1998; van den Oetelaar & Flipse, 1997). The friction and contact conductance data were acquired within the bounderies of a single island, thus avoiding multiple-contact points.

Fig. 4(a) shows a large number of I-V curves recorded at different loads up to 1.7 μN, using an 88 N/m cantilever. The I-V characteristics are semiconductor-like and consistent with the *p*-type doping of the diamond sample. The shape of the I-V curves remains basically constant at all loads, strongly indicating that the applied load does not significantly affect the surface electronic properties of the interface. This observation supports our assumption that the current is proportional to the contact area.

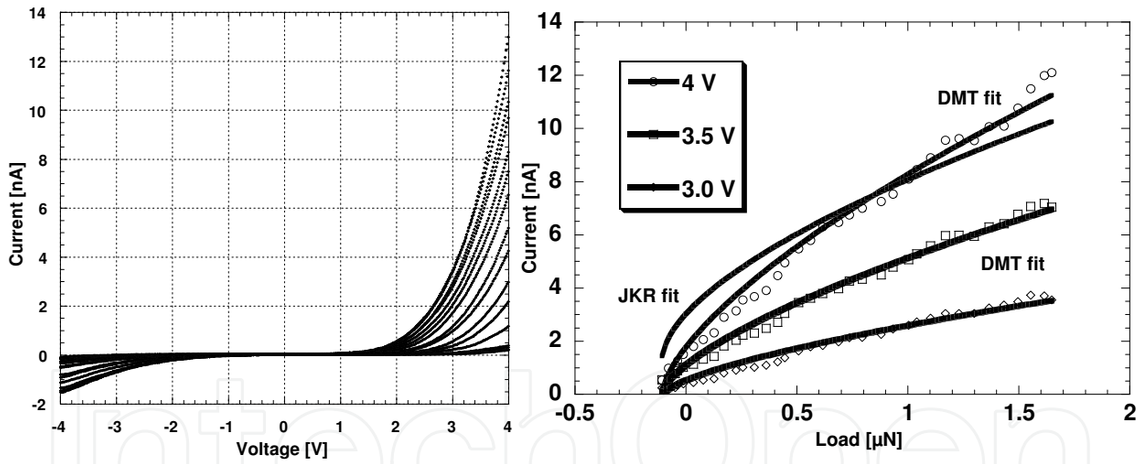

Fig. 4. (a) Current measured through the tip-sample contact versus bias voltage (I-V curves) recorded as a function of increasing load up to 1.7 μN. (b) Current versus applied load at three different constant bias voltages. The DMT fit is significantly better than the JKR fit, as illustrated for a bias voltage of 4 V, also indicated by the mean square deviation of the JKR fit, which is more than one order of magnitude worse for the JKR fit compared to the DMT fit.

Plotted in Fig. 4(b) is the load dependence of the current at several bias voltages applied to the sample, e.g., +3 V, +3.5 V and +4 V. The data can be fit by the DMT model, using Lc as a free parameter. The DMT model provides an excellent fit to the measured data, and the value of L_c deduced from the fits is in excellent agreement with the independently measured pull-off force of -0.1 μN, obtained from cantilever-sample retract experiments for the same cantilever.

The current versus load data was fitted using the JKR model. Treating L_c as a free parameter, the JKR fits, at all bias voltages, predict a critical load which is systematically and substantially too small compared to the independently measured pull-off force. If we apply the constraint L_c = -0.1 μN to the JKR fit, the resulting fit is clearly incompatible with our data, as illustrated in Fig. 4(b) for a bias voltage of 4 V. In addition, we found from the fitting statistics that the mean square deviation of the JKR fit is more than one order of magnitude worse than that of the DMT fit. These local contact conductance results clearly show that the load dependence of the contact area for this single-asperity interface can be described by the DMT continuum mechanics model.

A topographic AFM image is actually a convoluted image of the tip and surface features of the sample. Usually, one requires sharp AFM-tips to reveal the surface topography, but similarly, an extremely sharp feature on the surface can provide information about the shape of an AFM-tip (Atamny & Baiker, 1995). To determine the radius of curvature of the tungsten-carbide coated tip used in our friction experiments, we performed scans over the sharp edges of a faceted $SrTiO_3$(305) sample (Sheiko et al., 1993) in air. The surface is terminated with a large number of (101) and (103) facets, which form long sharp ridges that are suitable for tip imaging (Carpick et al., 1996a; Ogletree et al., 1996; Sheiko et al., 1993). The thus obtained cross-sectional "image" of the AFM-tip actually provides an upper limit to the tip dimensions, but this upper limit appears to be very close to the real tip dimensions (Carpick et al., 1996a). The cross-sectional tip-profile can be fit by a hemisphere, as is shown in Fig. 5, resulting in a radius of curvature of 110 nm. Profile analysis using the $SrTiO_3$(305) sample was performed before and after tip-sample contact, and no evidence of wear was discerned.

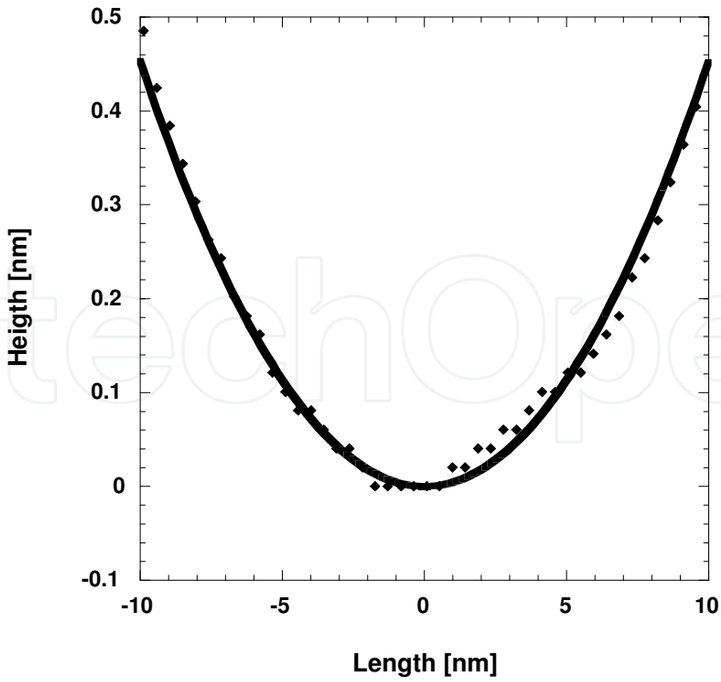

Fig. 5. Hemispherical fit of the AFM-tip profile, resulting in a radius of curvature R = 110 nm. Note the difference in vertical versus horizontal scale.

Having obtained a value for the tip radius R, we can estimate the empirical parameter μ. Using $L_c = -2\pi\gamma R$, γ can be obtained from the measured pull-off force. A typical normal force versus cantilever-sample displacement curve, during retraction of the cantilever, is shown in Fig. 6. The corresponding pull-off force is -7.3 nN, resulting in $\gamma = 0.01$ J/m^2. Thus, using z_0 = 2 Å, E_{diamond} = 1164 GPa (Klein, 1992), E_{WC} = 700 GPa (Shackelford et al., 1994), ν_{diamond} = 0.08 (Klein, 1992), and ν_{WC} = 0.24 (Shackelford et al., 1994), we find that μ = 0.02. Indeed, this value is much smaller than the DMT condition $\mu < 0.1$ discussed above, showing that the present tip-sample contact is firmly in the DMT regime.

Friction experiments were performed as a function of applied load using the soft lever (Enachescu et al., 1998). They were reproducible at different locations on the sample, and were obtained by decreasing the load from 12 nN to negative loads (unloading). Experiments where the load was increased (loading) exhibited the same behavior as the unloading results, indicating that the deformation of the contact is elastic for the range of loads investigated.

Friction versus load experiments could be fit very well by the DMT model, while treating both γ and the shear strength τ as free parameters (Enachescu et al., 1998). The mathematical fit results in a pull-off force of -7.3 nN and a shear strength of 238 MPa. Thus, the pull-off force predicted by the DMT fit is in excellent agreement with the pull-off value measured experimentally, as shown in Fig. 6.

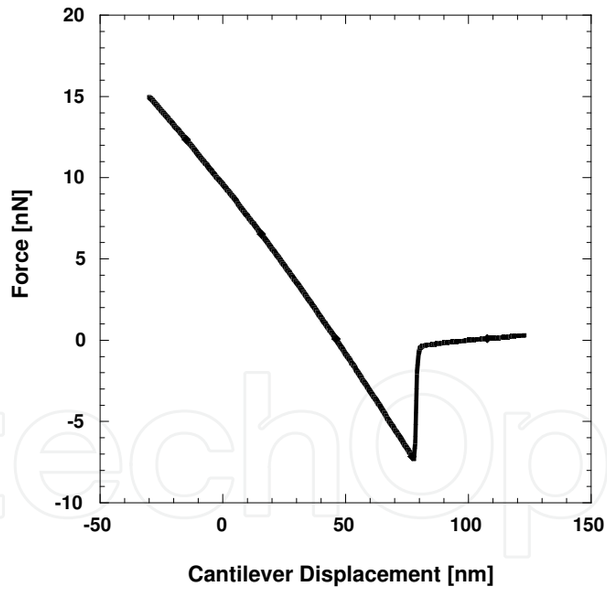

Fig. 6. Typical normal force versus cantilever-sample displacement curve, during retraction of the cantilever. The corresponding pull-off force is –7.3 nN.

The measured pull-off force actually represents an *independent* verification of the DMT fit, since γ (and thus also the pull-off force) was treated as a free parameter in the DMT fit. Attempts to fit the JKR model to the friction versus load curves, using L_C both as a free parameter and as a constrained parameter, produced strongly inconsistent fits. Experimentally, no friction data for loads smaller than -2 nN could be obtained due to a

premature pull-off of the tip. This premature pull-off is promoted by the tip-sample movement during scanning and is more likely to appear in this particular experiment due to the very low adhesive force between the surfaces in contact.

In an attempt to learn more about the relation between the friction force and the area of contact, we have plotted the friction force versus contact area, and the result is shown in Fig. 7. The friction force plotted in this figure is exactly the friction force measured during friction versus load experiments. The contact area was calculated using the DMT theory. The use of the DMT theory is supported by the three previous pieces of experimental evidence, namely: (i) the excellent DMT fit of the current versus load data using the stiff lever, presented in Fig. 4(b); (ii) the excellent DMT prediction of the Tabor parameter, $\mu < 0.1$, calculated after experimental determination of the radius of curvature R of the tip presented in Fig. 5, and of the pull-off force L_C presented in Fig. 6; (iii) the excellent DMT fit of the friction versus load experiments and the independent confirmation of the DMT fit by the experimental value of L_C presented in Fig. 6. Following the procedure suggested and supported above we found that a linear fit is the optimum fit for our friction force versus contact area representation in Fig. 7, demonstrating that, indeed, $F_f = \tau A$. Consistently, this free linear fit intercepts the origin, and the slope is a measure of the shear strength. We find that the shear strength τ = 238 MPa, a value which lies within the typical range for AFM experiments (Carpick & Salmeron, 1997).

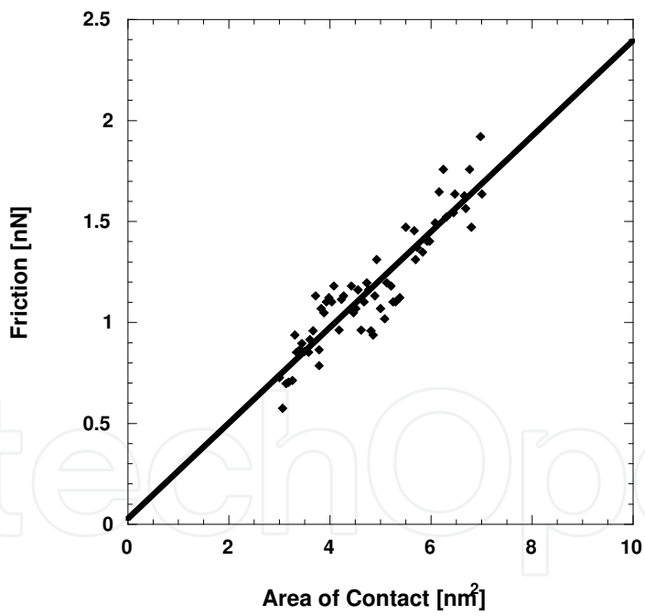

Fig. 7. Friction force versus contact area, showing a clear linear relation. The corresponding shear strength τ = 238 MPa.

So, in contrast to the macroscopic law of friction, the friction force at the interface of a single-asperity is directly proportional to the contact area. Furthermore, since friction does not depend linearly upon the applied load for a single-asperity contact, one should be careful defining a friction coefficient, *i.e.* the friction force divided by the normal force, in AFM experiments, as its value varies with load.

The constant shear strength that we observe indicates that the mechanism of energy dissipation for this system does not change in this pressure range. Thus, the increase in friction with load is attributable to the increase in contact area, *i.e.* more atoms in contact, as opposed to a change in the frictional dissipation per interfacial atom. This may not be so surprising given that the nominal stress is only increasing as roughly $L^{1/3}$ (from the continuum mechanics models). The most likely mechanism of energy dissipation is thermalization of phonons generated at the contact zone during sliding. New modes of energy dissipation, resulting from inelastic processes, may activate at higher stresses (Carpick & Salmeron, 1997). For example, evidence of tip-induced atomic-scale wear has been reported for alkali-halide materials (Carpick et al., 1998b). Pressure-activated modes of energy dissipation are reported in organic thin films due to progressive molecular deformation (Barrena et al., 1999). These examples represent stress-dependent increases in the number of energy dissipation channels and are therefore manifested in increases in the shear strength compared with purely elastic, wearless friction.

Finally, we comment on the relative magnitude of the observed shear strength. The theoretical prediction for the shear strength of a crystalline material in the absence of dislocations is roughly given by $G/30$ (Cottrell, 1988), where G is the shear modulus. We can define an "effective" interfacial shear modulus $G_{eff} = 2G_{WC}G_{diamond}/\left(G_{WC} + G_{diamond}\right) \approx 380$ GPa . This gives, for the diamond/tungsten-carbide contact, $\tau \approx G_{eff}/1600$. The shear strength of this system is thus far below the ideal material shear strength (Hurtado & Kim, 1998). Previous AFM results of Carpick *et al.* (Carpick et al., 1996a; 1998b) and Lantz *et al.* (Lantz et al., 1997a; 1997b) observed shear strengths near the ideal limit. An ideal shear strength in the range of $G/30$ suggests a "crystalline" or commensurate interface that is free of dislocations, where the commensurability may be brought about by atomic displacements induced by interfacial forces. Our measured shear strength indicates that there may be very little atomic commensurability for the diamond/tungsten-carbide interface, which is plausible considering the high stiffness of these materials. More importantly, the hydrogen passivation of the diamond surface strongly reduces the adhesive force, and also the friction force. In fact, removal of the hydrogen passivation would result in a value for the shear strength which is much larger than the ideal theoretical prediction of $G/30$ (van den Oetelaar & Flipse, 1997).

3. Wear and third bodies in nanocontacts

We have investigated the nanotribological properties of a tungsten carbide tip in contact with a clean Pt(111) single crystal surface under ultrahigh vacuum conditions using scanning probe techniques. Because of the conductive nature of the cantilever and tip, we could alternate between contact atomic force microscopy (AFM) and non-contact scanning tunneling microscopy (STM) using the same probe. Several types of interfaces were found depending on the chemical state of the surfaces. The first type is characterized by strong irreversible adhesion followed by material transfer between tip and sample. This resulted in substantial amounts of material being transferred from the tip to the sample upon contact. This material often covered areas far exceeding that of the contact region. Low adhesion and no material transfer characterize a second type of contacts, which is associated with the presence of passivating adsorbates in both (full passivation) or in one of the two contacting surfaces (half-passivation). Half-passivated contacts where the clean side is the Pt(111)

sample gave rise to periodic stick-slip friction behavior with a period equal to the atomic lattice constant of the Pt(111) surface. Local electrical conductivity measurements show a clear correlation between electronic and friction properties, with Ohmic behavior on clean regions of the Pt surface and semiconductor-like behavior on areas covered with adsorbates.

Our results indicate that substantial material transfer may be an important and inevitable property of nanocontacts when one surface is highly reactive and the other surface is not thoroughly cleaned. Furthermore, this work establishes that stable STM imaging using a conductive cantilever is a reliable method for observing this effect, and for observing fine features on clean portions of a reactive surface. In addition, the correlation between adhesion, friction, and contact conductance allows one to discern the existence and certain properties of the transferred material, which demonstrates that multi-functional scanning probe techniques are desirable for third-body processes at the nanoscale and nanotribology studies of tip-sample material transfer.

3.1 Background

The sliding of materials in contact often involves the transfer of material from one surface to the other. This material, referred to sometimes as the third body, influences the transient behavior of the sliding contact and can completely dominate the steady-state sliding behavior of many interfaces, especially for low friction coatings (Singer, 1992; 1998). Studies of low-friction materials such as diamond-like carbon coatings, MoS_2 coatings, and Ti-implanted steels indicate that chemically-modified transfer films are formed during initial sliding, and these films determine the long-term frictional behavior of the interface.

At small length scales third-bodies can also have a large impact on the contact properties. For example, hard disks and micro-electromechanical systems (MEMS) are critically limited by friction and adhesion-related failures due to the large surface-to-volume ratios of these devices (McFadden & Gellman, 1997). For such devices, an understanding of nano-scale third body behavior is important. Modeling work supports this notion. Robbins and co-workers have performed molecular dynamics simulations that indicate that molecular intermediate species in asperity contacts have a dramatic effect on friction (He et al., 1999; He & Robbins, 2001). They argue that contacts between crystalline or amorphous materials should, in general, exhibit very low friction due to the lack of interfacial lattice commensurability. The simulations show that molecules trapped at the interface, e.g. hydrocarbons, cause static friction that is consistent with observed macroscopic friction behavior.

The role of third bodies and transferred species at small scales is clearly worthy of further experimental study, specifically through the use of scanning force microscopy techniques. Already, fundamental insights into many aspects of friction have been obtained through the use of scanning force microscopy (Carpick & Salmeron, 1997). These studies have addressed several important topics such as atomic-scale stick-slip behavior, friction in the wearless (low-load) regime, friction in the presence of molecular lubricant films, the role of interfacial contact area, and wear initiation. However, there have been few studies of third body effects and transferred species. One example is the work by Qian et al. (Qian et al., 2000) who showed that in atomic force microscope (AFM) experiments, friction measurements exhibit transient behavior, where several tens of scans were required before friction behavior become reproducible. They proposed that the phenomenon is due to transfer of

material between the tip and sample, and observed that the mechanism of transfer depended on the relative humidity and applied load. Carpick *et al.* (Carpick et al., 1996b) observed that the frictional shear strength and interfacial adhesion energy of a Pt/muscovite mica interface in ultrahigh vacuum progressively decreased with each scan, but recovered if the tip was "cleaned" by blunting it to expose fresh Pt. The authors suggested that potassium adsorbates transferred from the mica surface to the tip could explain the strong, progressive reduction of adhesion and friction observed in the experiment. Using the surface forces apparatus (SFA) Drummond *et al.* (Drummond et al., 2001) performed experiments where WS_2 nanoparticles were suspended in a tetradecane fluid, and then compressed and sheared between the two mica sheets of the SFA. They found that the nanoparticles formed a transfer film of nanometer-scale thickness on the mica that reduced friction appreciably.

In this work, we discuss the results of a study of a Pt (111)/tungsten carbide single asperity interface using a combination of ultrahigh vacuum (UHV) AFM and scanning tunneling microscopy (STM) techniques. Since both the Pt sample and the carbide tip are conductive, we were able to measure the local electrical conductance of the contact and the friction force simultaneously (Enachescu et al., 1998; 1999a). In addition, the conducting tip allows STM operation, whereby high-resolution non-contact images of the sample can be obtained before and after the contact experiments.

3.2 Experimental

The experiments were performed in a UHV chamber (base pressure 7 x 10^{-11} Torr), equipped with a home-built AFM (Dai et al., 1995), low-energy electron diffraction (LEED), Auger electron spectroscopy (AES), differentially pumped ion sputtering, and sample cooling and annealing capabilities. The Pt(111) single-crystal sample was cleaned by sputtering with Ar+ ions of 1 keV energy, both in hot conditions (600 ^{0}C) and at room temperature, for 10-20 min. After sputtering O_2 was introduced in the chamber at 10^{-6} Torr for ~3 min while the sample temperature was kept at 600 ^{0}C. O_2 exposure and heating were then stopped. The cycle was repeated two or three times. Finally, the sample was flashed to 950-1000 ^{0}C for ~1 min. and cooled down at ~2 ^{0}C/sec. The AES pattern taken after the cleaning procedure indicated a clean Pt(111) surface, with the carbon peak at 271 eV not visible above the noise level, while platinum peaks at 237 eV and 251 eV are clear visible (Fig. 8). A sharp (1x1) LEED pattern was also observed (inset, Fig. 8).

Commercially available triangular silicon cantilevers with integrated tips, coated with approximately 20 nm of tungsten carbide, were used for all measurements. The cantilevers were characterized by scanning electron microscopy (SEM) in order to determine tip and lever dimensions, and also by AES to determine the chemical composition of the lever and tip shaft. The measurements showed the presence of both tungsten oxide and carbide, which is not uncommon for such coatings. For convenience we will refer to these as "tungsten carbide" tips. The similar chemical composition of the lever and tip is quite normal, as the WC coating is covering not only the tip but also the cantilever. For *such conditions* one may suggest that tip cleanliness is similar to the cantilever cleanliness, i.e., both covered with tungsten oxide and carbide. However, for our AFM/STM measurements most of the time the tip cleanliness is *not* similar to the cantilever cleanliness, as we often clean the AFM-STM tip and thus, removing the tip contaminant.

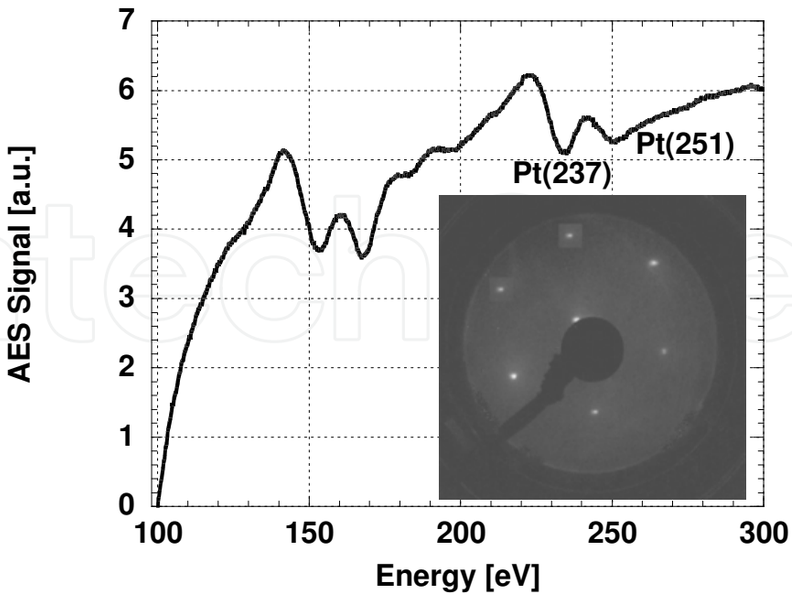

Fig. 8. AES spectrum showing the clean Pt(111) surface, e.g., platinum peaks at 237 eV and 251 eV are clear visible . Inset: a LEED pattern displaying the a clear Pt(111)-(1x1) pattern.

Two cantilevers with different spring constants of 88 N/m and 3.1 N/m were used. The stiffer cantilever was used for conductance and friction measurements while the other was used for certain high resolution friction measurements only. The tips were cleaned in UHV immediately prior to the measurements, by applying short voltage pulses and/or by rubbing them against the surface. Normal cantilever force constants were taken from the manufacturer, and the normal/lateral force ratio was calculated using the method described in (Ogletree et al., 1996). The absolute accuracy of the forces measured is limited due to significant uncertainty in the material properties of the cantilever and approximations used in the force constant calculations. However, relative changes in friction could be accurately determined by using the same cantilever and tip during a series of measurements. A large dynamic range, two-stage I-V converter was built, which provided a large frequency range while achieving sufficient gain. For this work, lower I-V gains (*e.g.*, 10^4) were used to measure the current flowing through the tip-sample junction while in AFM-contact mode, higher gains (*e.g.*, 10^9), were used for tunneling microscopy using the AFM tip.

3.3 Results and discussions

3.3.1 Irreversible adhesion between clean interfaces

As mentioned above, the Pt(111) sample was cleaned by sputtering and annealing, and its state checked by AES and LEED to verify the chemistry and structure of the surface. Because of the nanoscale dimensions of the tip apex, we could not assess spectroscopically its chemical state in the UHV chamber. However, we found that scanning at high loads on sacrificial areas of the sample consistently produced tips with highly adhesive properties and metallic conductance characteristics. Thus, rubbing a contaminated WC tip on a *clean metal* surface is an effective way to clean the tip. The adhesion force for tips prepared in this manner was large enough that even at the lowest load scanning was not possible without

severe damage. These contacts were characterized by means of force-displacement curves, as in the example shown in Fig. 9, where a pull-off force of L_c = 12.0 ± 1.2 μN was measured with the cantilever of 88 N/m normal spring constant. Assuming, for simplicity, an *elastic* adhesive contact, this force can be related to the work of adhesion of the interface. Within the extremes of the Johnson-Kendall-Roberts (JKR) model (Johnson et al., 1971), and the Derjaguin-Muller-Toporov (DMT) model (Derjaguin et al., 1975), we obtain an "effective" work of adhesion between 12 and 16 J/m². For this calculation, we used a value of 160 ± 20 nm for the tip radius, which was measured experimentally by scanning over sharp edges of a faceted $SrTiO_3$(305) sample (Carpick et al., 1996a).

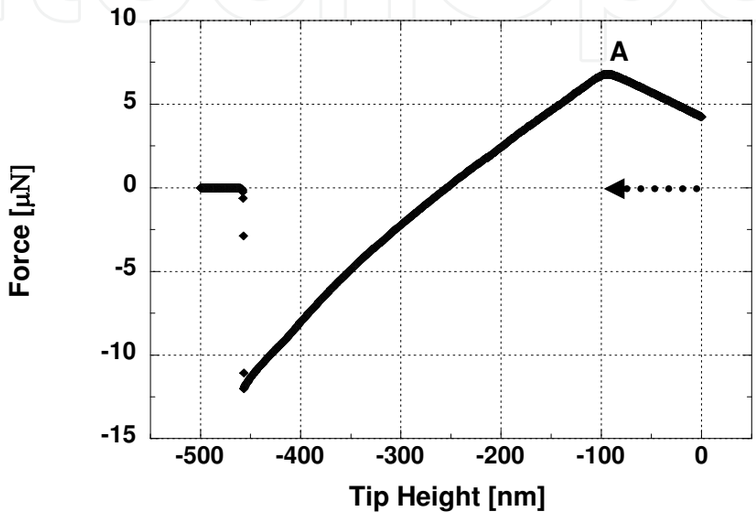

Fig. 9. Force-displacement curve for a tungsten carbide tip in contact with a clean Pt(111) sample. The plot is shown for the retracting portion only. The load appears to increase when retraction starts, even thought the tip-sample separation is increasing. This is due to the strong adhesion of the tip to the surface, which prevents sliding. Consequently, the tip pivots about the contact point. After that, the load decreases down to the pull-off point, as is usual in force-displacement curves. The deformations of the cantilever giving rise to this behavior are illustrated in Fig. 10.

This adhesion energy is likely an overestimate because we have neglected the possibility of plastic failure of the junction between the tip and sample. It is extremely difficult to apply such a model to this contact without knowing more about the contact geometry or the species at the interface. In any event, this effective work of adhesion is three orders of magnitude higher than that found in previous UHV AFM measurements (Carpick & Salmeron, 1997), such as 0.02 J/m² between silicon nitride AFM tips and the muscovite mica surface in UHV, or 0.4 J/m² for a Pt tip on a mica surface in UHV (Carpick et al., 1996b). Note that the surface energy of most metals is in the range of 1 to 5 J/m², i.e., 2 to 10 J/m² are required to split an ideal crystal in half to create two new surfaces (Israelachvili, 1992). Our value of 16 J/m² is beyond this range, consistent with the notion that we have likely overestimated the adhesion by assuming elastic contact. Nevertheless, our measurement indicates that we have observed extremely strong adhesion for this pair of materials. This indicates that strong bonds, at least several eV per atom suggestive of covalent bonds, are formed between the clean Pt(111) surface and the tungsten carbide tip.

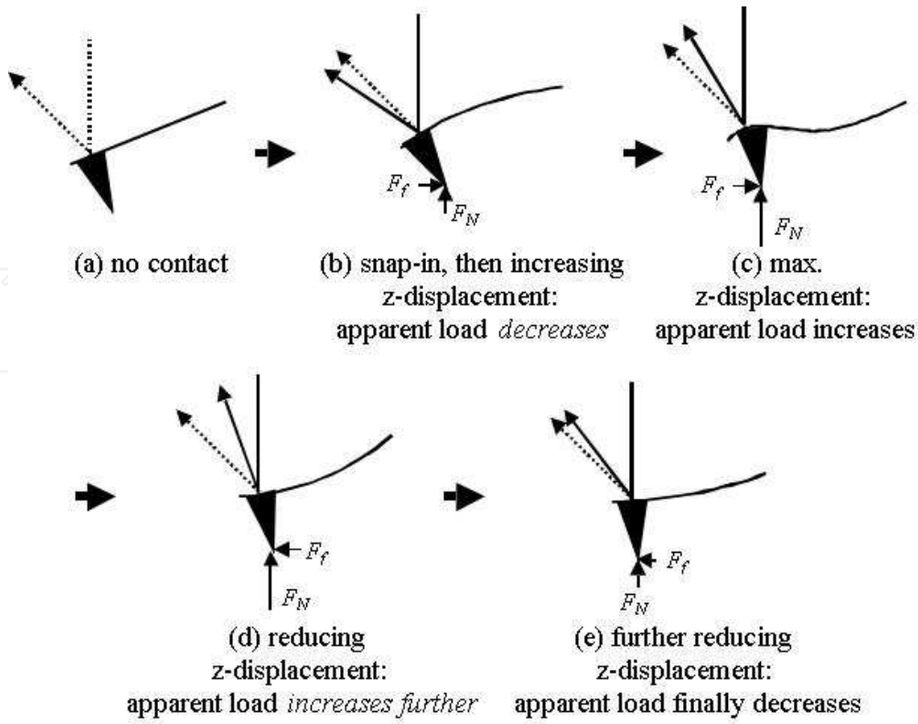

Fig. 10. Schematic drawing illustrating the deformation of a cantilever subject to high friction forces. (a) The cantilever is shown at the upper left for the case of no load. The dashed line represents the trajectory of the laser for the zero load case, and is included in all subsequent sketches. (b) After snapping into contact, the *z*-displacement is increased. Normally this would cause an increase in the laser signal (after the initial decrease due to the snap-in). But large friction forces cause bending at the end of the lever in the opposing direction, and producing an apparent *decrease* in the load. Friction is preventing the tip from sliding relative to the surface. (c) As the *z*-displacement is further increased, the friction force eventually reaches its limiting value. The tip will begin to slide relative to the surface, and the upward bending induced by the *z*-displacement overtakes the tendency to bend in the opposite direction induced by the friction force, so now the apparent load begins to increase. Eventually the *z*-displacement reaches a maximum value. (d) As the z-displacement direction is reversed, the friction force will now resist motion in the opposite direction, and so the bending it induces causes an apparent increase in the load. During this phase, the tip is not sliding relative to the surface. (e) Eventually the friction force reaches a limiting value and once again the tip begins to slide. The apparent load will now decrease as the *z*-displacement is decreased. Stages (d) and (e) are clearly evident in Fig. 9.

In addition, an unusual hysteresis feature in the force-displacement plots was observed at the largest z-displacements as seen in Fig. 9. The recorded data begins with the tip initially in contact after being pushed back by approximately 450 nm. As the cantilever is retracted, the apparent force on the cantilever *increases*, then eventually begins to decrease, as one would normally expect. This result can be explained by considering the effect of friction on the cantilever bending due to the tilted geometry with respect to the plane of the sample (22.5° in this case). Friction causes the cantilever to bend in addition to bending due to the normal force between the tip and sample. The direction of the bending will depend on the

direction of the friction force, which always acts to oppose any tendency for sliding. These two forces compete by changing the slope of the cantilever in opposite directions. This is illustrated in Fig. 10. Because of the strong bonding, the tip cannot slide over the surface and the cantilever is forced to adopt an S-shape like the one shown in Fig. 10(c). As the sample is retracted and the lever reverts to its normal bending shape (shown in Fig. 10(d)), it produces an apparent increase in the force initially. After passing through a maximum (point A in Fig. 9), the force decreases as expected. This effect is explained by the strong friction force on a cantilever fixed at one end and with a tilted geometry with respect to the plane of the sample (22.5° in this case). The slope of the force-displacement curve is inverted because static friction prevents the tip from sliding with respect to the surface. Instead the tip is pivoting about the contact point, and the slope of the end of the cantilever is increasing. Eventually the tip pivots enough that the maximum static friction force is reached and the tip can slide relative to the surface. Stages (d) and (e) sketched in Fig. 10 are evident in Fig. 9.

The fact that this hysteresis phenomenon is observed for a very stiff lever, *i.e.* a spring constant with two to three orders of magnitude higher than the typical contact AFM levers (88 N/m), indicates that strong friction forces are occurring in tandem with the strong adhesion forces. In addition, our experiments show a much stronger interaction between the AFM tip and the metallic surface compared to the results published by Bennewitz *et. al.* (Bennewitz et al., 1999; 2001). Those measurements involved silicon AFM levers having a spring constant of 0.024 N/m in contact with clean a Cu(111) surface under UHV conditions.

3.3.2 Contacts between fully passivated interfaces: Friction and conductance measurements

As we have seen with clean tips and clean surfaces, contact-mode measurements cannot be performed without severely disrupting the contact region. To perform contact experiments while avoiding strong modifications, the surfaces must be chemically passivated. This can be achieved intentionally or unintentionally by the presence of adsorbate layers. In our case we used the unintentionally passivation, provided without effort by the contaminant's presence, i.e., the contamination behaved like a "passivation" layer for the tip-sample interaction. An interesting question is whether these layers must be present on each or on only one of the surfaces for substantial passivation. The latter case implies that the layers are attached strongly to one of the surfaces and interact only weakly with the other, such that the contact can shear at this weak interface. As we will show in this and the next section, it is indeed possible to have both situations, which we shall call fully passivation when layers of material are present on each contacting surface, and half passivation, when one of the two surfaces remains clean, during and after friction scanning.

On the Pt surface, the most common contaminant after annealing in UHV is carbon, as verified with AES. On the WC tip, in addition to oxygen present as a tungsten oxide, adventitious hydrocarbon or graphitic carbon can also accumulate. Ex-situ AES on the body of the cantilever and on the tip shaft did indeed reveal the presence of O, C and W as the only observable constituents. We will first examine results where the Pt surface is covered by a layer of C-contamination, the only impurity element detected in the Auger spectra. Force-displacement data obtained with such passivated surfaces show low adhesion values in the range of ~1 J/m^2, depending on the spatial location of the tip over the surface, as shown in the example of Fig. 11.

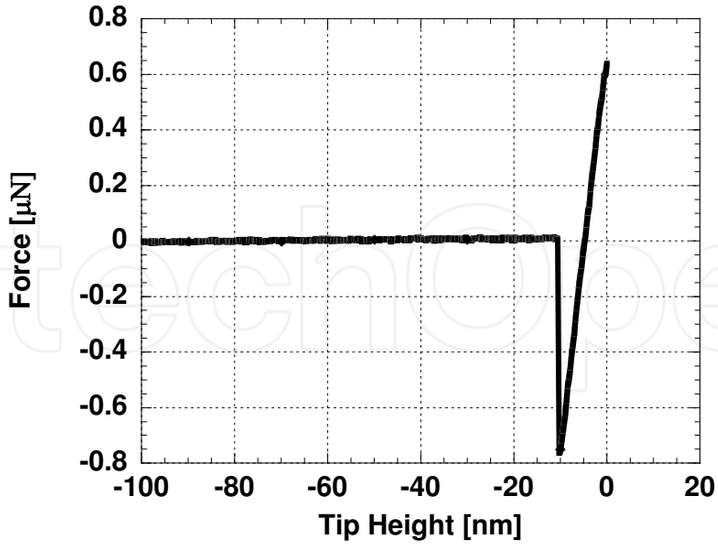

Fig. 11. A force-displacement plot for the same lever as in Fig. 7, but taken over a passivated area of the Pt(111) sample. The adhesion force is much lower, and the unusual behavior in the plot due to friction forces is not present.

Topography, friction, and point contact current (corresponding to contact conductance) were recorded simultaneously as the tip was scanned over the surface, (Enachescu et al., 1999b) as shown in Fig. 12(a,b). The friction and conductivity maps exhibit a strong correlation, with regions of high and low friction corresponding to regions of high and low electrical conductivity respectively. We propose that high friction and high local conductivity are associated with "cleaner" interfaces, while low friction and low local conductivity correspond to regions covered with more interfacial adsorbates. The spatial distribution of friction and conductance values remained consistent throughout several images. This indicates that the tip was not changing during the image acquisition, but rather, different regions of the sample had different amounts of adsorbates present.

Typical I-V characteristics obtained with contacts in areas with different degree of passivation are shown in the graphs of Fig. 12(c). We acquired current-voltage (I-V) curves in a 16 x 16 grid, while for each I-V curve the voltage was scanned from -50 mV to +50 mV. Ohmic behavior curves (straight lines) were always observed in the regions exhibiting high friction, while semiconductor-like behavior (sigmoid shapes) were observed in low friction areas. This observation can be understood on the basis of the poor conductivity of the contamination layers present, which decreases as their quantity, and thus passivation capacity, increases.

3.3.3 Contacts with half-passivated interfaces: Atomic lattice resolution images

In contrast with the fully passivated interfaces, when the Pt surface is clean, we could frequently observe stick-slip behavior with the atomic-lattice periodicity of the Pt(111) substrate, as shown in the image of Fig. 13(a) and the trace of a friction line in Fig. 13(c). The Fourier transform of the image (Fig. 13(b)) shows more clearly the 3-fold symmetry with 0.27 nm periodicity, in agreement with the lattice constant of Pt(111). The image was acquired under zero externally applied load. The occurrence of stick-slip behavior was always

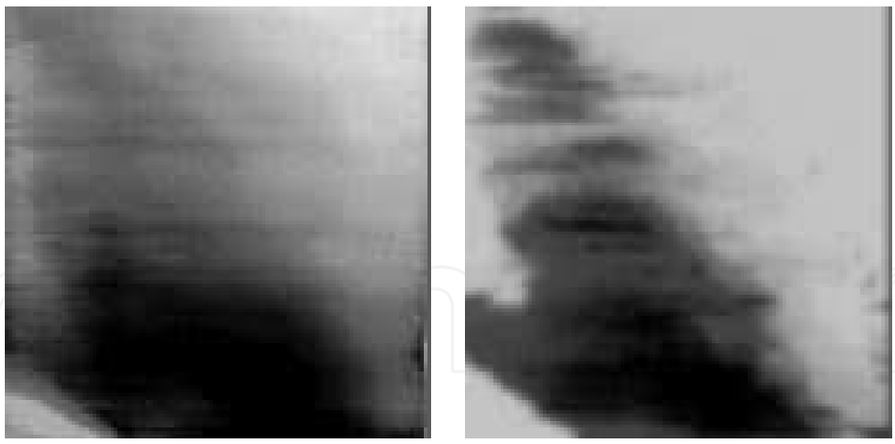

(a) (b)

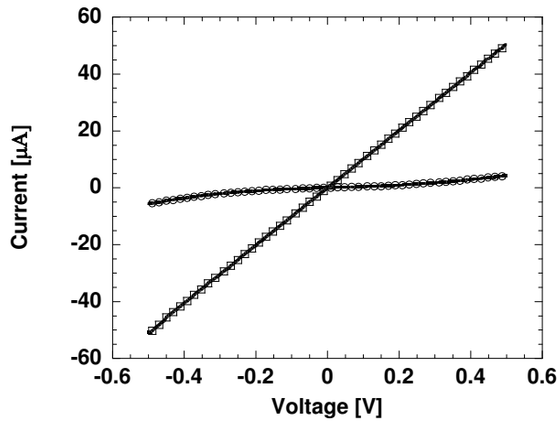

(c)

Fig. 12. Simultaneous friction (a) and point contact current (b) images of a Pt(111) surface acquired with a conductive WC-coated Si cantilever of 88 N/m spring constant. Image size is 500 x 500 nm^2. Regions with high and low friction are clearly correlated to regions of high and low local conductivity. (c) Corresponding *I-V* spectra acquired at the points of "clean" and "passivated" areas. The bias between tip and sample was varied from -50 mV to +50 mV. High friction regions are correlated with Ohmic conductance behavior, while the lower friction regions exhibit non-Ohmic conductance, indicative of an insulating or semiconducting interlayer.

associated with the presence of low adhesion, low friction, and low contact current, indicative of chemically inactive tip. These atomic stick-slip images were recorded by carefully choosing flat terrace locations. We did not scan areas that included steps, in order to avoid the increased reactivity of the step sites.

This result indicates that the passivating layers are on the tip side of the interface, where they are bound strongly enough to withstand the applied shear stresses without transference to the Pt surface. In contrast to these unintentional adsorbates used as passivation layer, other intentional, well-defined adsorbates may not be well bound as to the WC tip and thus, may not provide any additional understanding to the tip-metal interaction we described in this work. An analysis of the energy balance during friction is of interest here.

Since the friction force is approximately 190 nN, the energy dissipated after a displacement of one unit cell (~3 Å) is about 350 eV. Given the tip radius of 160 nm, and a total load of ~0.8 μN (see Fig. 11) a contact area of roughly 100 nm² can be calculated containing approximately 1000 atoms. This corresponds to an average energy dissipated per atom of 0.3 eV. We would predict that this energy is not enough to break the strong chemical bonds of the Pt atoms, and indeed that is what we observe.

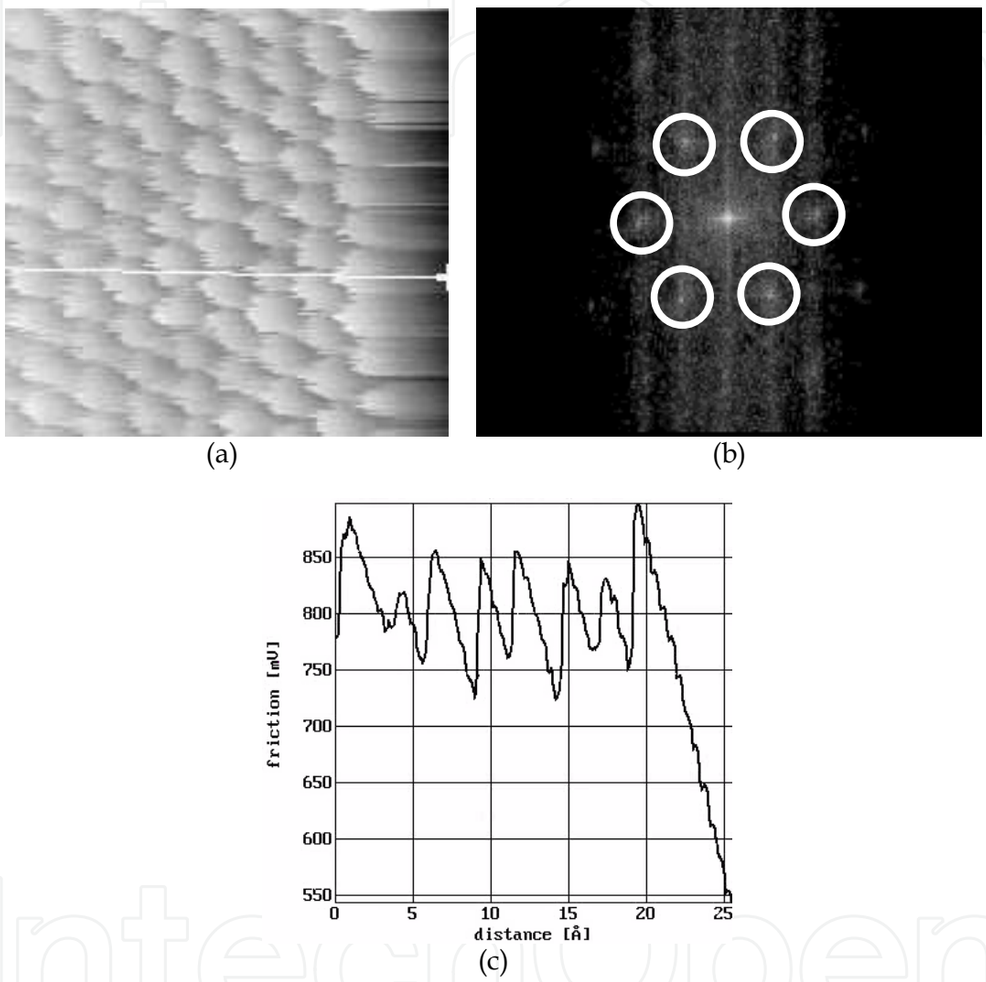

Fig. 13. (a) 2.5 x 2.5 nm² lateral force image obtained with a passivated tip and a clean Pt(111) sample. Atomic-lattice stick-slip friction is clearly observed and provides proof that sliding is taking place along a clean Pt surface; (b) Fast Fourier transform of the data in (a), showing the periodicity and symmetry of the Pt(111) surface; (c) line trace of the line indicated in (a) showing the clear stick-slip behavior.

3.3.4 Tunneling experiments using the AFM tip

In most cases the adhesion between the AFM tip and the Pt(111) was so strong that we were not able to scan the tip over the sample and often the fracture of low spring-constant AFM cantilevers was observed. Reproducible scanning over the Pt(111) surface was only possible when a small amount of contaminant was present between the tip and the sample.

To further investigate the Pt(111) surface we performed non-contact scanning tunneling microscopy (STM) experiments using the conductive WC AFM tip. For these experiments the AFM cantilever must be sufficiently stiff, otherwise the cantilever will jump into contact (Carpick & Salmeron, 1997; Enachescu et al., 1998) before or during tunneling conditions at small physical gaps, *e.g.,* 0.7-1.0 nm. We used an 88 N/m stiff lever, which was enough to avoid the jump to contact.

Fig. 14 shows an STM image acquired with an AFM lever prior to any tip-sample contact. The 200 nm x 200 nm image was acquired with a bias of 0.1 V (sample negative) and a tunneling current of 160 pA. Several monoatomic steps, with a height of 0.22 ± 0.01 nm, and terraces are visible. A few isolated protrusions are also observed on the terraces and also attached to the step edges. They correspond probably to contamination. The round flat islands attached to the steps have a height of 0.1 nm and clearly pin the steps, which would have been flowing during the high temperature anneal.

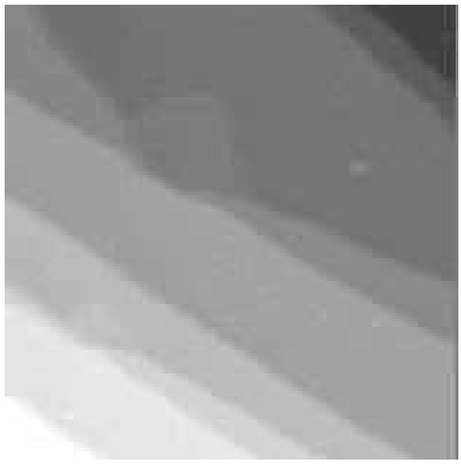

Fig. 14. 200 x 200 nm^2 STM image of the Pt(111) surface taken *before* any contact has been made between the tip and sample. A series of single atom steps, 0.22 ± 0.01 nm in height, are observed. Two of the steps are seen to be pinned by contamination, which is likely carbon that has diffused to the surface region from the bulk during processing of the crystal. The image was acquired for an I-V converter gain of 10^8 under the following tunneling condition: tunneling bias of 0.1 V (sample negative) and a tunneling current of 160 pA.

Fig. 15 shows a 200 x 200 nm^2 STM image acquired with the AFM lever *after* mechanical contact has been made between the tip and sample. Specifically, the tip was brought into contact with the sample and then retracted. The tip was not scanned during this contact. The tip was then brought back to within tunneling range and used to acquire the STM image with a bias of -0.2 V and a tunneling current of 160 pA. Large, irregular features up to 13.7 nm in height are seen covering roughly 75% of the image. In the topmost 25% of the image Pt(111) steps can still be seen. This image demonstrates that the bonding of the tip to the surface was very strong, and that rupture of the contact occurred within the tip material itself. This material is then left over the Pt surface.

Another example of STM imaging followed by contact and AFM imaging and then again STM imaging is shown in Fig. 16. The 100 nm x 100 nm image in (a) was acquired at a bias of -0.2 V and tunneling current of 200 pA and shows a stepped region of the Pt(111) surface

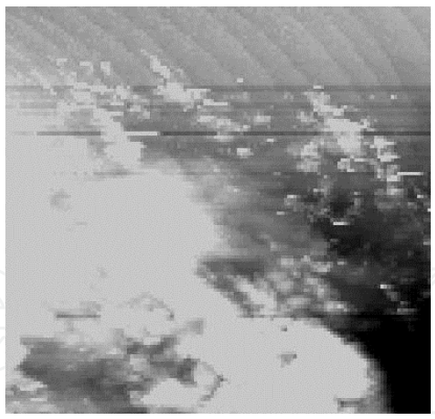

Fig. 15. STM image of the Pt(111) surface after AFM mechanical contact has been made between the tip and sample. The 200 x 200 nm² STM image was acquired with a tunneling bias of -0.2 V and a tunneling current of 160 pA, while the I-V converter was operating at a 10^8 gain.

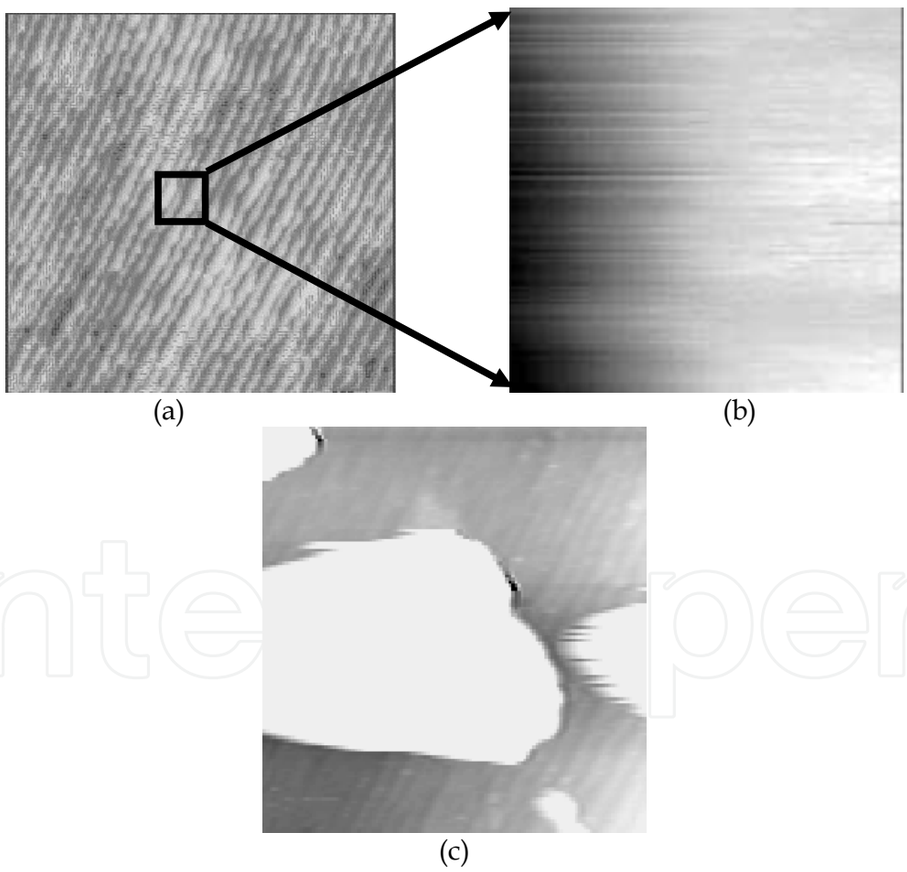

(a) (b)

(c)

Fig. 16. (a) 100 x 100 nm² STM image of a highly stepped region of the Pt(111) surface. The image was acquired under the following tunneling conditions: bias = -0.2 V; current = 200 pA; (b) 10x10 nm² AFM friction force image acquired in contact at the center of (a); (c) Subsequent STM image, acquired under the same conditions as in (a), showing substantial material deposition from the AFM tip during the previous contact

before contact. Fig. 16(b) shows a 10x10 nm^2 AFM contact friction force image at zero externally applied load acquired in the center of Fig. 16(a). During imaging the bias was held at zero volts. High friction forces are observed in this image. The tip was then withdrawn from contact and another STM image acquired, shown in Fig. 16(c), under identical tunneling conditions as Fig. 16(a). It is obvious from Fig. 16(c) that substantial material deposition from the AFM tip during contact scanning process has taken place.

Using the friction force during slip of several μN, the energy dissipated during imaging can be estimated to be of the order of 10^8 eV. The amount of material left on the surface (Fig. 16(c)) occupies an area of roughly 2,500 nm^2. The energy dissipated during friction is therefore sufficient to break the junction, even if very strong (~5 eV) bonds need to be broken.

4. Local conductivity in nanocontacts: The integration of point-contact microscopy

The electrical current through the point-contact junction of an AFM tip was used to image the surfaces of bulk graphite (HOPG) and the surface of a graphitized carbon monolayer on Pt(111) under ultra-high vacuum (UHV) conditions. Lattice-resolved images were obtained simultaneously in topography, lateral friction, and contact current channels. Lattice resolution in current maps persisted up to 0.9 mA and pressures of up to 5 GPa. In both bulk graphite and the case of graphitized carbon monolayer on Pt(111), the current images showed only one maximum per unit cell. In addition, the contact current images of the graphite monolayer revealed local conductivity variations. We observed local conductivity variations in the form of moiré superstructures resulting from high order commensurability with the Pt lattice.

4.1 Background

Since the invention of the scanning tunneling microscope (STM) (Binnig et al., 1983), graphite, specifically highly-oriented pyrolytic graphite (HOPG), has become a popular substrate due to its flat cleavage surface and its inert nature, which makes it possible to obtain images in air with "atomic resolution" (Hansma, 1985) (Binnig et al., 1986b). However, the literature reports a number of well-known puzzling features, such as uncharacteristically large corrugation amplitudes (Binnig et al., 1986; Selloni et al., 1985; 1986; Tersoff, 1986; Batra & Ciraci, 1988; Batra et al., 1987; Soler et al., 1986), enhanced lateral resolution (Binnig et al., 1986; Selloni et al., 1985; 1986; Tersoff, 1986; Batra & Ciraci, 1988; Batra et al., 1987; Soler et al., 1986; Park & Quate, 1986), a weak dependence of the tunneling current on the position of the tip in the direction perpendicular to the surface (Salmeron et al., 1991), and anomalously large superperiodicities (Kuwabara et al., 1990). These features generated a debate about the imaging mechanism. In most STM images, one observes only one maximum per unit cell, indicating that the carbon atoms are not imaged as individual units. In a favored explanation, the lattice periodicity is due to the tip imaging a single electron state of the graphite layer (Tersoff, 1986). STM images taken on one monolayer of graphite deposited on metals also show only the lattice periodicity, and not single atomic positions (Land et al., 1992a; 1992b).

In the debate concerning the imaging mechanism of HOPG in STM, it was suggested that the STM tip could be in contact with the HOPG. In order to clarify this issue, Smith *et al.*

(Smith et al., 1986) performed an experiment imaging the HOPG surface by purposely placing the tip in contact with the surface. In contact, the situation is similar to that in point-contact spectroscopy (Yanson et al., 1981). This mode of microscopy was called point-contact microscopy (PCM) (Smith et al., 1986), which differs from STM in that the tip is much closer to the sample in the region where the potential barrier is significantly reduced and tip-sample forces are repulsive. In this mode, Smith *et al.* succeeded in imaging the HOPG lattice by measuring the current flowing through the contact. However, they were able to report lattice resolution only at low temperatures, *i.e.,* when the microscope was immersed in liquid helium. Since their contact area involved a large number of atoms, they explained the "atomic" resolution by considering the conduction to be due to a single atom on the tip, which we now consider unlikely. Other experimental evidence indicates that true tunneling through a vacuum gap might not occur in the case of graphite in normal circumstances, and that the tip is in contact with the surface (Salmeron et al., 1991).

In AFM contact mode, lattice resolution can be obtained both in topography and friction channels. This is usually explained as the result of stick-slip phenomena (Marti et al., 1987). AFM measurements involving a conductive lever have been reported (Lantz et al., 1997a, 1997b; Enachescu et al., 1998) in conjunction with tip-sample contact area evaluation. To date, there have been no reports of AFM contact experiments on graphite deposited on metals.

This work presents results on the simultaneous implementation of AFM and PCM techniques by using a conductive AFM lever. We demonstrate the possibility of obtaining lattice resolution concurrently in three channels: topography, friction, and contact current. This is achieved by using both HOPG and 1 ML of graphite deposited on a Pt(111) single-crystal. We show that PCM is as capable of similar lateral resolution as contact AFM imaging. We also found that PCM is sensitive to local conductivity variations due to moiré superstructures resulting from the high order commensurability of the graphite and Pt lattices at different relative rotations. Moreover, we show that lattice resolution in PCM mode is achievable for currents of up to 0.9 mA and contact pressures estimated at 5 GPa.

4.2 Experimental

All experiments were performed in a UHV chamber (base pressure 7 x 10^{-11} Torr) equipped with AFM, Auger Electron Spectroscopy (AES) and Low-energy Electron Diffraction (LEED) (Dai et al., 1995). Two different samples, HOPG and Pt(111), were used. The HOPG sample was cleaved along the (0001) plane in air and then immediately placed in the vacuum chamber.

The samples could be heated by means of electron bombardment from a hot dispenser cathode. The Pt sample was prepared using standard procedures of Argon ion bombardment, oxygen treatment, and annealing until a clean and ordered surface was produced, as verified by AES and LEED. The clean surface was then exposed to ethylene at room temperature by backfilling the chamber with ethylene. Exposures were typically greater than 10 Langmuir to ensure saturation of the Pt(111) surface. After exposure, the sample was heated to about 1250K, resulting in the decomposition of ethylene and formation of a single monolayer of graphite on the Pt(111) surface. When observed with LEED, we found that the graphite layer produced characteristic fragmented rings (Hu et al.,

1987), with several dominant bright segments. Some of the ring segments were in-line with the Pt spots, indicating alignment or near-alignment of the graphite and Pt lattices. Others were at an angle relative to the Pt spots, indicating that the graphite lattice was rotated with respect to the Pt lattice.

We measured derivative Auger spectra of the surface with an RFA-type electron analyzer, using a normally incident electron beam with an energy of 2500 eV and retarding field oscillation amplitude of 7 eV peak-to-peak. The ratio of the peak-to-peak heights of the carbon (275 eV) and platinum (237 eV) AES transitions in the derivative spectrum was found to be about 3.8, independent of the amount and method of ethylene exposure. We attribute this to saturation of the surface once a graphite monolayer is formed, such that no further decomposition of ethylene can take place. Because of this, we concluded that there was 1 ML of graphite on the Pt(111) surface. This conclusion is supported by Land *et al.* (Land et al., 1992a, 1992b), who determined by STM, under similar preparation conditions, that the deposited graphite layer was 1 ML thick.

All experiments were performed with a silicon cantilever with a spring constant of 3.5 N/m, and coated with a ~20 nm thick conductive tungsten-carbide layer (bulk resistivity ~30 μΩ-cm). The tips were characterized by Scanning Electron Microscopy (SEM) and AES. Previous UHV-AFM measurements on a Pt(111) sample showed that similar tungsten-carbide coated tips are wear resistant and conductive (Enachescu et al., 1998, 1999b). The tips were treated in UHV immediately prior to the measurements by applying short voltage pulses while in contact and/or by rubbing them at high loads on the surface. We designed and built a flexible I-V converter that allowed us to measure high contact currents by taking measurements spanning the range from pA to mA.

4.3 Results and discussions

4.3.1 Topography, friction, and current imaging

Fig. 17 shows three 2.5 nm x 2.5 nm images of the HOPG surface, which were acquired simultaneously. The feedback control was turned off in order to avoid the convolution of topography and friction, and to minimize noise. The images correspond to: (a) normal lever deflection, (b) lateral force or friction, and (c) contact current. A positive bias of 1.0 V was applied to the sample, and the external load during imaging was 100 nN. The average current in (c) was 0.94 μA, with a modulation of about 17%. In all three images, the 0.246 nm graphite lattice periodicity is clearly observed. Using the DMT contact mechanics model (Müller et al., 1983; Derjaguin et al., 1975), with a measured pull-off force of 115 nN, we estimate that our contact radius is 4.1 nm, and therefore contains about 2000 atoms. The contact radius calculated here is only approximate, since the Tabor parameter (Greenwood & Johnson, 1998; Tabor, 1977) for this system is 0.67, which indicates that the DMT model is not entirely appropriate. Moreover, none of the analytical contact mechanics models are directly applicable to a non-isotropic material such as graphite (Sridhar et al., 1997).

Similar lattice-resolved images were obtained on 1 ML of graphite on Pt(111) (Gr/Pt(111)). An example of this is shown in Fig. 18. As in the previous case, the 2.5 nm x 2.5 nm images correspond to: (a) normal lever deflection (under feedback-off conditions), (b) lateral force, and (c) contact current. The external load in this case was 300 nN, and the sample bias was 0.5 V. The average current was 52.7 μA, with a current modulation of about 2%. In this case,

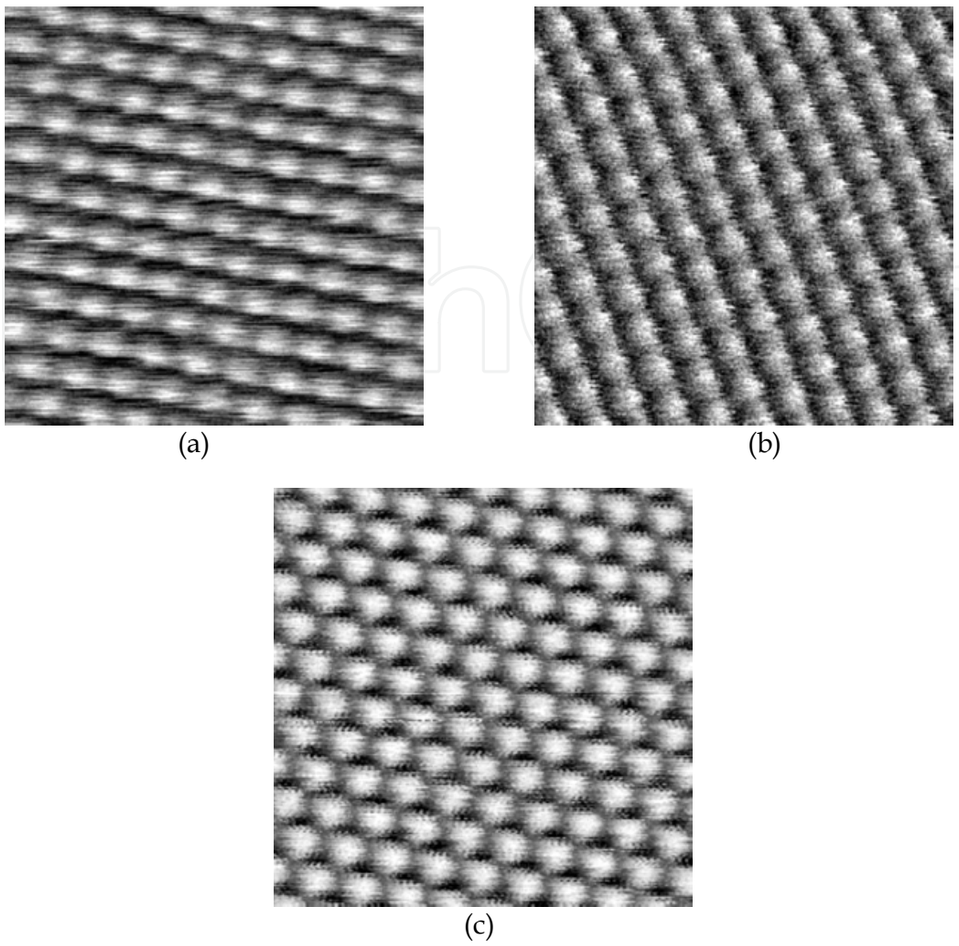

Fig. 17. Simultaneously acquired lattice resolution images of HOPG under UHV conditions: (a) normal lever deflection (with topographical and buckling effects), with a corrugation of 117 pN, corresponding to a height of 33.6 pm; (b) lateral friction image, average force of 0.5 nN and corrugation of 20 nN; (c) PCM image, average current of 945 nA and peak-to-peak corrugation of 160 nA. Image was taken with an applied load of 100 nN without feedback. Image size is 2.5 nm x 2.5 nm.

the diameter of the area of contact was similarly estimated to be 5.78 nm, which contains approximately 4000 atoms. Here the 0.246 nm graphite lattice periodicity is also clearly revealed. We were able to obtain lattice resolution at currents up to 0.9 mA and high load. The average pressure at high load was approximately 5 GPa, which is less than the theoretical yield stress of Pt (~17 GPa). At pressures higher than 5 GPa and/or currents higher than 0.9 mA, the images were unstable, although the graphite lattice was still visible.

As a side note, we found that we were able to obtain lattice resolution almost all the time and immediately in current mode, while lattice resolution was not as readily visible in the topography and/or friction channels. In many cases, the friction was so low that there was no stick-slip present, *i.e.,* the tip moved continuously over the graphite layer. Because of these reasons, we can rule out the atomic stick-slip mechanism as a reason for the lattice resolution observed in PCM mode.

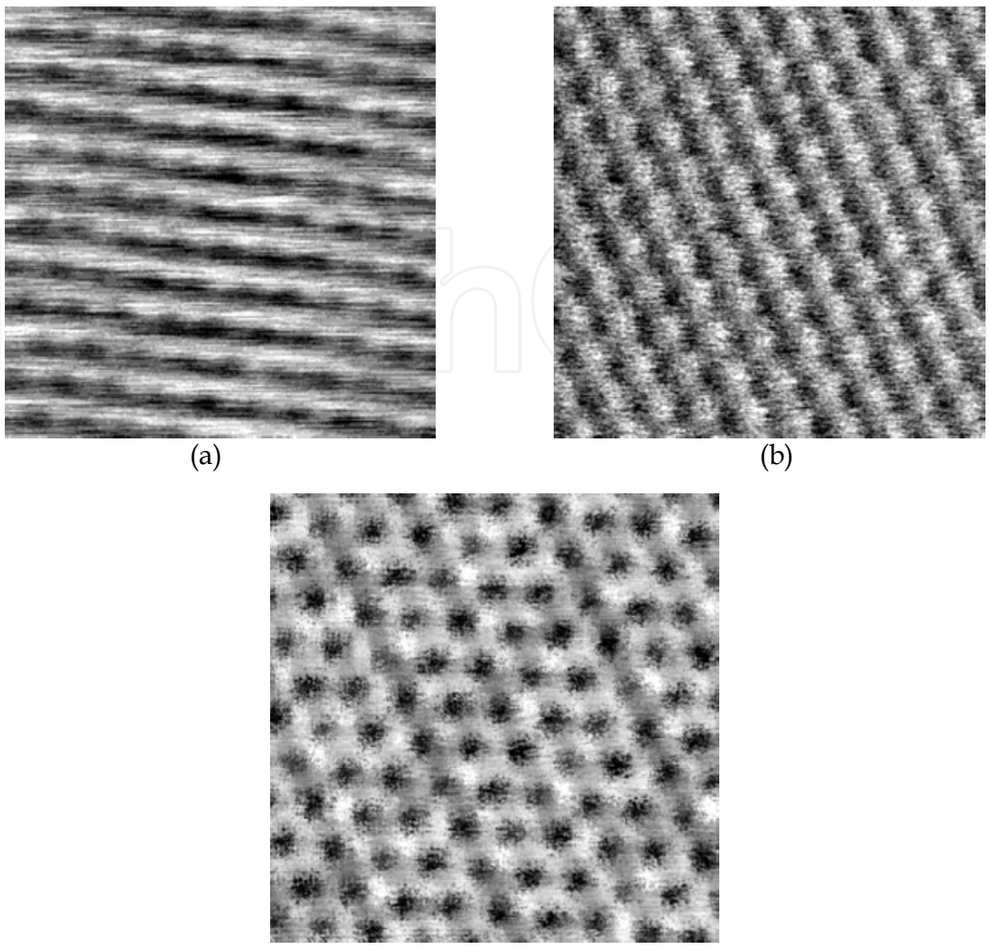

Fig. 18. Simultaneously acquired lattice resolution images of 1 ML of graphite deposited on Pt(111) in UHV: (a) normal lever, corrugation of 164 pN; (b) lateral friction image, average force of 0.4 nN and corrugation of 17 nN; (c) PCM image, average current of 53 μA and peak-to-peak corrugation of 1.1 μA at a bias of 0.53 V. Image was taken with an applied load of 300 nN without feedback. Image size is 2.5 nm x 2.5 nm.

4.3.2 Moire´ structures

It is known that, for similar preparation conditions (Land et al., 1992a; Hu et al., 1987), graphite forms several orientational domains on a Pt(111) sample. Depending on the preparation conditions and annealing temperature, different sizes and orientations of domains can be prepared. In Fig. 19, we show a 60 nm x 60 nm image of two graphite domains on Pt(111).

The hexagonal periodicity observed in the upper left domain in this image is about 2.0 nm. The large unit cell arises from the superposition of the incommensurate lattices of graphite and Pt(111) at a particular angle. In higher resolution images of this domain, such as the one shown in Fig. 20, the graphite lattice of 0.246 nm, together with the larger 2.0 nm cell, is revealed. Using the real space image and its 2-D Fourier transform, we find that the

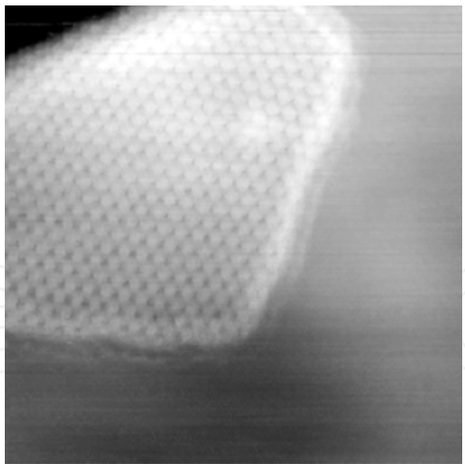

Fig. 19. PCM image showing two moiré superstructure domain on graphite/Pt(111). The upper left has a periodicity of ~2.0 nm, and the superstructure lattice was determined to be ($\sqrt{63}$ x $\sqrt{63}$)R19 with respect to the graphite lattice. Image size is 60 nm x 60 nm. The other domain in this image is (5 x 5) with respect to the graphite lattice, although it is not resolved at this scale.

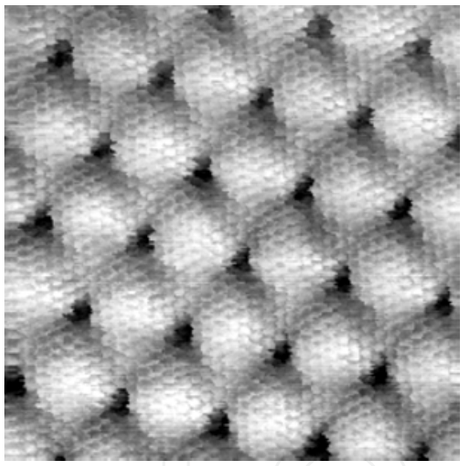

Fig. 20. Close-up image of the ($\sqrt{63}$ x $\sqrt{63}$)R19 domain in Fig. 19, showing the graphite lattice, as well as the moiré superstructure. Image size is 10 nm x 10 nm. Average current is 90 μA and corrugation is 5 μA at a bias of 0.8 V.

structure in Fig. 20 corresponds to a superstructure with a ($\sqrt{63}$ x $\sqrt{63}$)R19 unit cell with respect to the graphite lattice. Contrary to standard usage, we report on the moiré structures with respect to the overlayer instead of the substrate, since we can directly count the number of graphite unit cells in the moiré superstructure. Using the known lattice constants of graphite and Pt and the measured angles, we can calculate that the moiré periodicity is almost exactly 7 Pt lattice spacings, and the moiré cell is rotated by 22° with respect to the Pt lattice. Indeed, one can create the 2.0 nm periodic superstructure by rotating the Pt [1-10] direction with the graphite [1010] direction by 2.68°, as shown in Fig. 21. There is a small lattice misfit of 0.60 % associated with the coincidence of the graphite

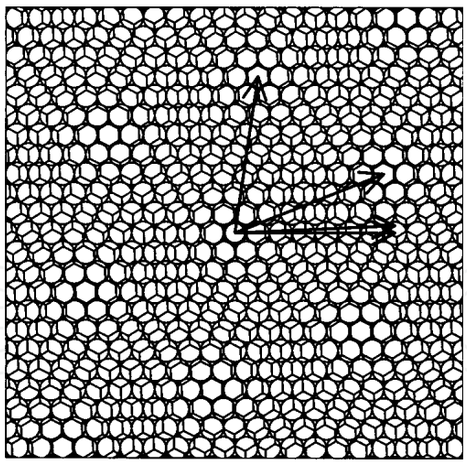

Fig. 21. Schematic of the ($\sqrt{63}$ x $\sqrt{63}$)R19 (with respect to graphite) moiré domain superstructure. With respect to the Pt(111) substrate, the moiré domain is (7 x 7)R22. The Pt atoms are shown as circles with a scaled diameter equal to the lattice constant of Pt (0.278 nm). The graphite lattice is shown as hexagons in which carbon atoms are located at the vertices with C-C distance of 0.142 nm and lattice constant of 0.246 nm. Vectors are drawn to indicate the orientation of the two lattices and the moiré domain. Image size is 5.5 nm x 5.5 nm.

lattice at 1.954 nm and the Pt lattice at 1.942 nm, which can be accounted for by a corresponding relaxation of the graphite layer or the platinum substrate.

Other graphite domains having different orientations and moiré superstructures have been observed, frequently adjacent to each other. The image in Fig. 22 shows three contiguous graphite domains, each having different orientations. It is interesting to note that the average current in these domains is different, even if all other conditions (bias, load, tip structure) are the same. The average current can also vary appreciably inside a single domain, such as at a platinum step, as we discuss below.

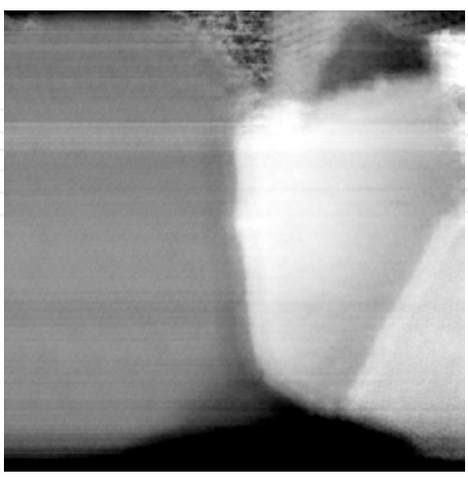

Fig. 22. PCM image showing different moiré domains. Image size is 100 nm x 100 nm. Note that the average current is different on each domain. Average currents are 86, 100 and 97 μA for the left, center and right domains, at a bias of 0.8 V.

At higher magnification, different periodic superstructures on each domain can be seen. The image in Fig. 23, which was obtained from the left domain of Fig. 22, shows a (3 x 3) modulation of the graphite lattice. Its 2-D Fourier transform is shown in Fig. 24. The larger hexagonal pattern, marked by six circles, corresponds to the 0.246 nm graphite lattice, while the smaller hexagon, marked by squares, represents the 0.738 nm superstructure lattice. The calculated angle of the graphite lattice with respect to Pt(111) lattice is 19.1°, which is in agreement with the measured angle.

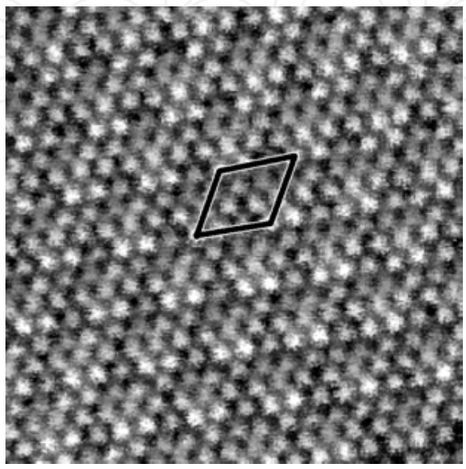

Fig. 23. PCM image of a (3 x 3) moiré superstructure, showing the graphite lattice. Image size is 5 nm x 5 nm. Average current is 79 μA and modulation amplitude is 0.93 μA at a bias of 0.7 V.

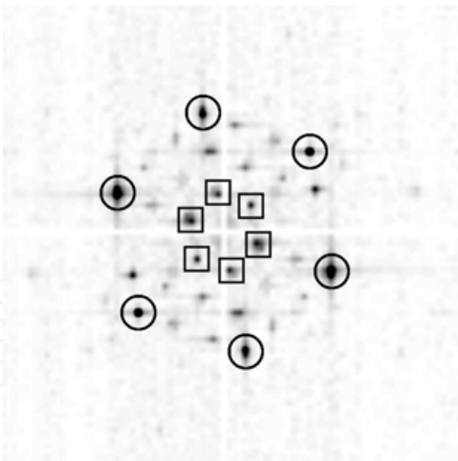

Fig. 24. Fourier transform of image in Fig. 23, showing the graphite lattice periodicity of 0.246 nm marked by circles, and the moiré superstructure periodicity of 0.738 nm marked by squares.

The domain in the middle of Fig. 22 has a (5 x 5) modulation of the graphite periodicity, as shown in the 5 nm x 5 nm image of Fig. 25. In this moiré structure, the angle between the graphite and the Pt(111) lattices is calculated to be 23.4°. The domain in the lower right of Fig. 22 was identified as a ($\sqrt{31}$ x $\sqrt{31}$)R9 structure.

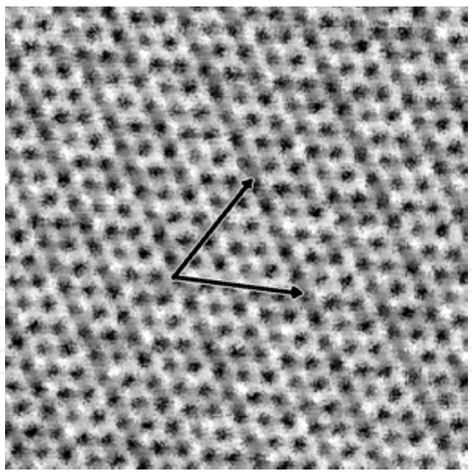

Fig. 25. Close-up image of a (5 x 5) moiré superstructure, showing the graphite lattice. The arrows indicate the moiré lattice. Image size is 5 nm x 5 nm.

Table 1 is a list of the experimentally observed moiré structures. Using the ratio of the lattice constants of graphite and Pt, we were able to calculate near-coincidences of the graphite and Pt lattices at different angles, and thus predict the existence of all of the structures.

Moiré periodicity relative to graphite	Moiré periodicity relative to Pt(111)	Angle between graphite and Pt lattices [^{0}]	Moiré periodicity [nm]	Coincidence misfit [%]
(3x3)	(√7x√7) *R*19	19.1	0.738	0.60
(√19x√19) *R*23	(4x4)	23.4	1.07	3.4
(5x5)	(√19x√19) *R*23	23.4	1.23	1.7
(√31x√31) *R*9	(5x5)	8.9	1.37	1.2
(√52x√52) *R*14	(√43x√43) *R*8	21.5, 6.3	1.77	2.5
(√61x√61) *R*26	Unknown		1.92	< 4.0
(√63x√63) *R*19	(7x7) *R*22	2.7	1.95	0.60
(√73x√73) *R*6	Unknown		2.10	< 4.9

Table 1. Moiré superstructures experimentally observed in PCM mode. Structures with respect to the Pt lattice are deduced from the measured structures on graphite. In certain cases, the angle of the Pt lattice was known, which aided in the extrapolation.

4.3.3 Measuring local conductivity using PCM

To determine the lateral resolution of PCM, we acquired images of regions containing platinum steps. We observed that the graphite layer covers the Pt steps continuously from the upper terrace to the lower adjacent one, as shown in Fig. 26. It is important to mention that the image in Fig. 26 is a contact current image. At distances far from the step in this image, the average current is the same on both terraces. However, close to the step, on what we have identified as the lower terrace, the contact current decreases by approximately 30%. At this scale, the topography image shows no contrast, since the graphite layer is almost flat,

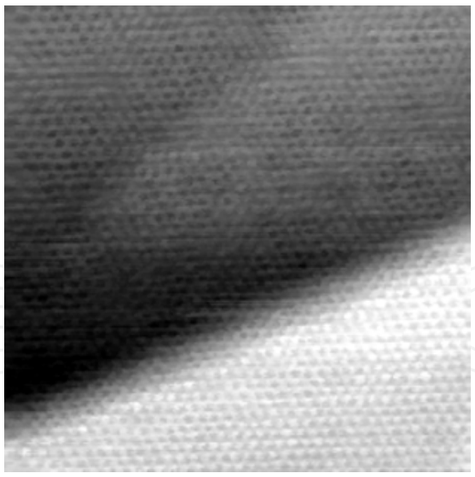

Fig. 26. PCM image of a Pt step covered by a continuous layer of graphite. The topography image (not shown) is completely flat, and does not reveal the presence of a step in the graphite layer at this scale. Image size is 10 nm x 10 nm. The average current is 39 μA on the upper terrace and 28 μA on the lower terrace at a bias of 1.0 V.

although tilted with respect to the Pt substrate. On larger scale images of regions containing wide Pt terraces, it is possible to measure a height difference between the terraces. The same (5 x 5) moiré superstructure was detected on both sides of the Pt step, which indicates that a continuous sheet of graphite is covering the step.

In these experiments, we noticed that the tip-sample contact is not always conductive, unlike in previous experiments with similar cantilevers (Enachescu et al., 1998), possibly because of contamination as a result of gases used during sample preparation. In particular, when such contamination is observed, current vs. load curves indicate that the current is often not proportional to contact area, with a weak dependence on load, much less than would be expected from contact area variations. The step observed by PCM in Fig. 26 is about 1.5 nm wide, denoting a lateral resolution in PCM mode of this value. Using the DMT contact mechanics model as we did earlier, we estimate that the diameter of the contact area is approximately 8 nm, which indicates a contact AFM lateral resolution of no less than 8 nm. We can use the Sharvin model for point-contact resistance (Sharvin, 1965; Wexler, 1966) and the measured point-contact resistivity to estimate the area through which current flows in our contact. The diameter of this area is estimated to be 0.9 nm, which is consistent with the observed lateral resolution in the PCM image.

One explanation for our observation of the different resolutions in AFM and PCM is that the tip is covered with a poorly conducting layer, which is partially broken when the tip is cleaned by applying voltage pulses. This phenomenon may be limited to the tungsten-carbide coating of the tip used in this experiment. Another explanation may be that only the highest-pressure region of the contact area contributes to the point-contact current. However, a graph of current vs. load strongly favors the former explanation. We note that the weak dependence of current on load indicated by these graphs resembles the similarly weak I-Z dependence observed in the past in STM experiments on graphite (Salmeron et al., 1991). This supports the idea that, in most cases, STM on graphite is actually point-contact imaging. The change in local conductivity over the Pt step is likely due to the increased

distance between the graphite layer and the underlying Pt substrate. The increased distance acts much like a tunneling barrier. In our measurements, we are able to measure current independently of topography, since the tip-sample contact is affected only by the mechanics of the system. The STM technique uses feedback on current to measure topography, so, for example, in the case of the blanketed Pt step, the STM tip would see the decrease in current and move closer to the sample to compensate. Thus, an STM image of a blanketed step would show a topographic step in the graphite layer with a width of 0.2 nm (i.e., typical STM resolution), while contact AFM indicates that the step width is many tens of nanometers. This width is the distance from the platinum step where the graphite layer begins to separate from the platinum substrate. Since the PCM technique is capable of separating mechanical and electrical measurements, it can offer additional insight into the electronic and tribological properties of surfaces.

The STM images of Land et al. (Land et al., 1992a; 1992b) indicate that there is local conductivity modulation at both the lattice and the moiré periodicities. If we imagine the atoms in our AFM contact contributing to the contact current as a collection of STM tips, one for each atom, the total contact current would be the sum of the contribution of these tips. We would still expect to see both the lattice and the moiré periodicities in the resulting PCM image, although the magnitude of modulation relative to the average current would decrease. The modulation would sum to zero only in special, destructively interfering cases. This will be discussed in more detail in a future work.

5. Sensing of dipole fields force in scanning tunneling and force microscopy experiments

The electric field of dipoles localized at the atomic steps of metal surfaces due to the Smoluchowski effect were measured from the electrostatic force exerted on the biased tip of a scanning tunneling microscope. By varying the tip-sample bias the contribution of the step dipole was separated from changes in the force due to van der Waals and polarization forces. Combined with electrostatic calculations, the method was used to determine the local dipole moment in steps of different heights on Au(111) and on the 2-fold surface of an Al-Ni-Co decagonal quasicrystal.

5.1 Background

The different electronic structure of the atoms at steps and terraces of metal surfaces is thought to be responsible for their different (often-enhanced) chemical reactivity. Dipole moments are postulated to exist localized at the steps due to incomplete screening of the positive ion cores by conduction electrons, because the spatial variation of the charge density is limited by the Fermi wavelength. This is known as the Smoluchowski effect (Smoluchowski, 1941). Indirect support for this assumption is provided by work function (φ) measurements. Besocke and Wagner found a decrease in φ proportional to the step density on Au(111) (Besocke & Wagner, 1973) and used this to estimate the average value of the step dipole. Similar results have been reported for Pt(111) and W(110) (Kral-Urban et al., 1977l; Besocke et al., 1977). Calculations using the jellium model (Ishida & Liebsch, 1992) predict that the localized step dipole increases with step height and screening length. Electronic structure calculations for the (111) and (100) microfacet steps on Al(111) produced very small dipole moments (Stumpf & Scheffler, 1996), indicating that the Smoluchowski

effect alone is insufficient to fully describe the electronic structure of steps. It is therefore important that the presence and the magnitude of local dipole moments at steps be measured experimentally.

Scanning probe microscopy can be used to investigate the electronic structure of steps. Marchon *et al*. observed a reduction in the tunneling barrier at surface steps on sulfur-covered Re(0001) (Marchon et al., 1988) using scanning tunneling microscopy (STM). Later Jia *et al.* used this effect to calculate the step dipole for Au(111) and Cu(111) (Jia et al., 1998a; 1998b). Arai and Tomitori investigated step contrast as a function of tip bias on Si(111) (7x7) using dynamic atomic force microscopy (D-AFM) (Arai & Tomitori, 2000) and suggested that step dipoles could explain their observations. In contrast Guggisberg *et al.* investigated the same system using STM feedback combined with D-AFM force detection and concluded that the step dipole moments in Si(111)-(7x7) were negligible (Guggisberg et al., 2000). They attributed the D-AFM contrast effects to changes in the van der Waals and electrostatic polarization forces, which are reduced above and increased below the step edges relative to the flat terrace.

In this work we report measurements of the strength of the fields produced by the step dipoles through direct measurement of the electrostatic force they produce on biased tips. We use a combined STM-AFM system (Enachescu et al., 1998; Park et al., 2005b) with cantilevers that are made conductive by a ~30 nm coating of W_2C. Relatively stiff cantilevers of 48 or 88 N/m were used to avoid jump-to-contact instabilities close to the surface. Attractive forces cause the cantilevers to bend toward the surface during imaging, as illustrated in Fig 27(a). Scanning is done at constant current as in standard STM mode, while forces are measured simultaneously from the cantilever deflection (Park et al., 2005c).

The force acting on the tip is the sum of van der Waals and electrostatic contributions. The former is independent of the applied bias. The electrostatic contributions are additive and can be written as (Jackson, 1975):

$$F = f(D/R)V^2 + g(D/R)PV + h(D/R)P^2 \quad (1)$$

where D is the tip-surface distance, R the tip radius and *f*, *g* and *h* are functions of the tip and sample geometry. P is the dipole moment, and *V* is the electrostatic potential difference between tip and sample. The first term in (1) represents the attractive force from polarization (i.e. image charges) induced by the applied voltage. The second term is due to surface dipoles *P* interacting with the biased tip, and is proportional to the bias. The last term is the force between the dipole *P* and its image on the tip. Of these contributions only the second term is linear with applied voltage, and provides an easy way to determine the net effect of the dipole field.

5.2 Experimental

The measurements were carried out in ultra high vacuum with an optical deflection AFM. Several samples were used, including Pt(111), Au(111) and the two-fold surface of a $Al_{74}Ni_{10}Co_{16}$ decagonal quasicrystal prepared by cutting the crystal parallel to the ten-fold axis. The growth and characterization of the Al-Ni-Co quasicrystal are outlined in detail elsewhere (Fisher et al., 1999). Due to the aperiodic nature of the atomic layering in the latter sample, steps of various heights were readily obtained on a single surface. The Pt single crystal and the quasicrystal (Park et al., 2004) samples were sputtered and annealed in UHV.

The Au sample was in the form of a thin film on glass, prepared in air by flame annealing and transferred to vacuum without further treatment. An average tip radius of 30-70 nm was determined by SEM imaging.

5.3 Results and discussions

Figure 27(b) and 27(d) shows the STM topography and force image of Pt(111) obtained simultaneously for a tip bias of –0.2 V. Fig 27(c) is a height and force profiles across the line in (b). The force, which is always attractive, increases by ~1.5 nN as the tip approaches the bottom of the step and decreases by ~4 nN after climbing over the step. When the attractive force increases, the STM current feedback loop retracts the base of the cantilever to keep the tunnel current, and hence the tip-sample distance, constant. The reduction of attractive force in the upper side of the steps is due to the reduction in the van der Waals and polarization part of the force (image charges), since in that position half of the surface (the lower terrace) is farther away from the tip. This is consistent with the results of Guggisberg (Guggisberg et al., 2000). By itself this result does not prove the existence of localized dipoles at the steps. For that we need to examine the changes in the force due to applied bias.

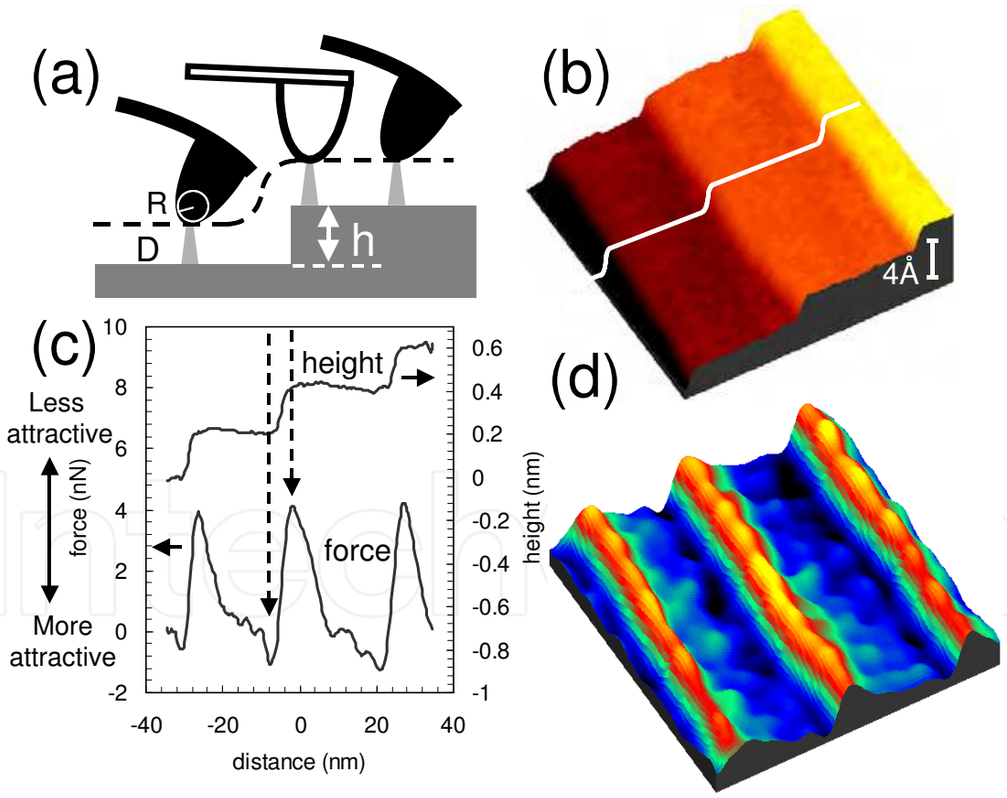

Fig. 27. (a) STM-AFM configuration using a conductive cantilever bending in response to forces. (b) 70 nm x 70 nm STM image of a Pt (111) surface (V_t = –0.2V, I=0.16nA). (c) Height and force profile across the steps. The force on the tip is more attractive at the bottom of the steps and less attractive at the top. (d) Force image simultaneously acquired with (b). Yellow and blue colors represent low and high attractive forces, respectively.

Earlier studies of decagonal Al-Ni-Co quasicrystal surfaces (Kishida et al., 2002) indicate that the bulk structure consists of pairs of layers with 5-fold quasiperiodic structure stacked along the 10-fold direction with a periodicity of 0.4 nm. In our 2-fold surface this produces rows of atoms arranged periodically. The rows are separated by distances varying in an aperiodic manner and are parallel to the step edges. Most steps have heights of 0.5, 0.8 and 1.3 nm, although a few are observed also with 0.2 nm. The ratios of these heights follow the golden mean (τ ~1.618), characteristic of their quasiperiodic nature. Fig. 28(a) shows a topographic profile perpendicular to the 10-fold axis, along with corresponding force profiles acquired at +1.2 and –1.2 V tip bias (at 100 pA tunneling current). Fig 28(b) shows similar topographic and force profiles across single and double-height steps on Au(111) at +3 and –3 V tip bias. Like in the Pt case, there is a reduction of the attractive force when the tip crosses over the steps (upward peaks in the force profile). While this reduction is present for both + and – bias, there is a noticeable difference between the two. The difference between forces at opposite biases eliminates all contributions except that from the second term in equation (1), which is purely due to the step dipole. We can immediately conclude that the positive end of the step dipole points up, consistent with a smaller attractive force at positive tip bias.

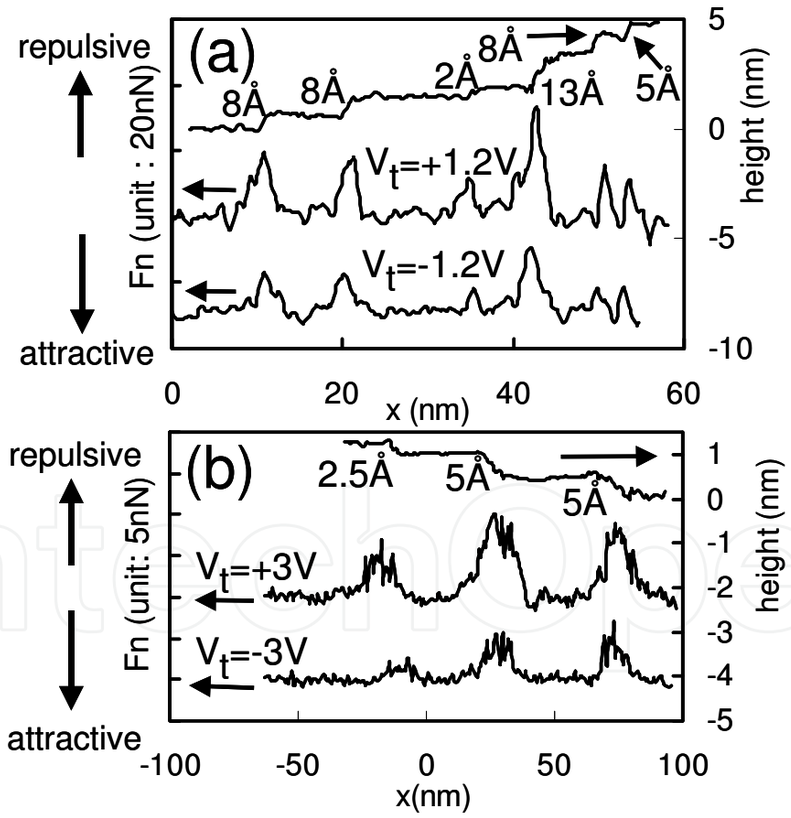

Fig. 28. (a) Height and force profiles across steps for positive and negatively biased tip (I = 0.1nA) on the Al-Ni-Co quasicrystal surface showing steps of multiple heights (0.2, 0.5, 0.8 and 1.3 nm). (b) Height and force profile across steps on a Au(111) surface. Small relative peak shifts in the force profiles are caused by noise and thermal drift. V_t is the tip voltage with respect to the sample.

Approach curves (force and current versus distance at fixed bias) were used to determine an STM tip-sample distance of 0.5 ± 0.1 nm during tunneling as shown in Fig. 29. Tunnel current vs. voltage curves for all samples showed a metallic character, with no significant dependence on bias polarity, so there is no change in the tip-sample distance under STM feedback when polarity is reversed. Force *vs* voltage curves over flat terraces reveal a small tip-sample contact potential difference of 0.14 V for the quasicrystal and 0.20 V for gold. This contact potential difference is negligible compared with the applied bias and cannot account for the polarity-dependent force contrast at step edges.

The tip radius can be extracted from the force-distance curves as described in previous work (Sacha et al., 2005) that shows that the effective tip radius is given by $R= 36A/V^2$, where A is the slope in the plot of electrostatic force F, versus 1/D, F is in nanonewton, 1/D in nm^{-1}, V in volts, and R in nm, as shown in the inset of Fig. 29.

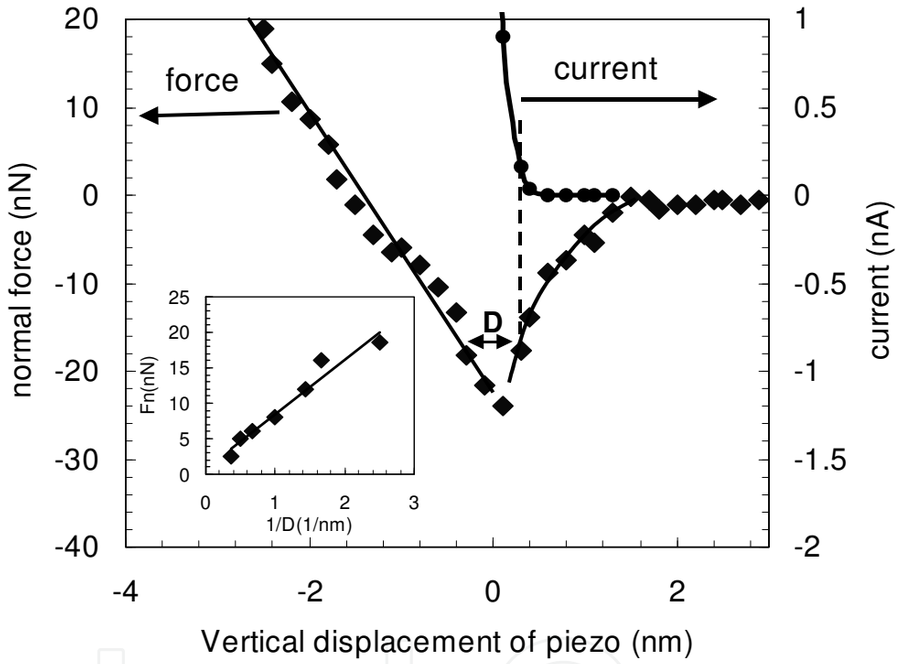

Fig. 29. Force and current-distance curves measured on Au(111) at a tip bias of –3V. Before contact the electrostatic force bends the tip towards the surface. This attraction is used to calculate the tip radius (inset), from the slope of F vs. 1/D, yielding R =30 nm.

Results from measurements using the polarity-dependent component of the force (i.e., the difference between forces at V^+ and V^- bias, divided by 2|V|) at steps of various heights are shown in figure 30(a). As can be seen, the experimental points follow a straight line. To determine the magnitude of the step dipole moment, we compute the electrostatic force using the *Generalized Image Charge Method* (GICM) program (Mesa et al., 1996; Gómez-Moñivas et al., 2001), a variational method for solving electrostatic problems that is particularly efficient for problems with high symmetry. The tip is modeled by a sphere of radius R, which is an equipotential surface produced by a series of point charges q_i and dipoles p_i at fixed positions r_j within the sphere. The magnitudes of the charges are adjusted to reproduce the boundary conditions of a constant potential V at radius R, and the sample surface at ground. With a

suitable choice of positions, a relatively small number of point charges (less than 10) can reproduce the potential over the surface of the sphere within ~1%. In this method the relative positions of the point charges and dipoles within the tip are fixed; only the magnitudes of the charges are changed as the tip-sample geometry is changed.

For the present geometry, six point charges were distributed along the surface normal between the center and the sphere boundary, plus two symmetrical pairs of point dipoles located off-axis in the plane defined by the surface normal and the line dipole P. Once the effective charges were determined, the tip-sample forces were calculated as the sum of the forces between the point charges q_i, p_i, their image charges q_i', p_i' below the surface plane, and the fixed line dipole P. The field distribution calculated using these parameters is shown in Fig. 30(b).

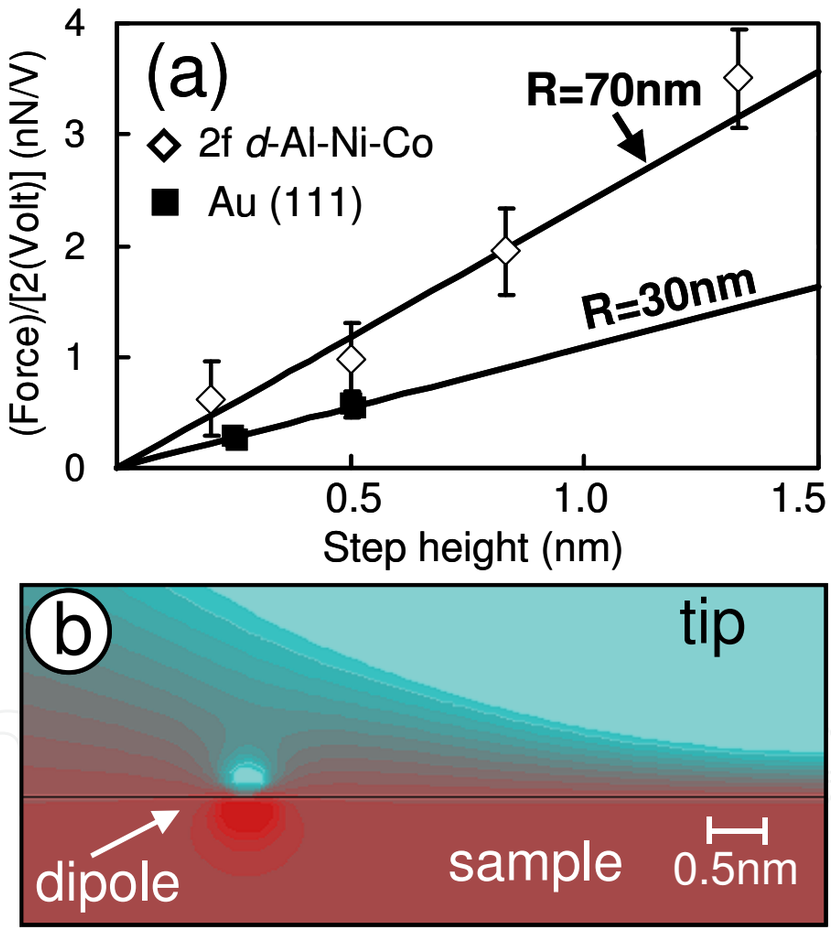

Fig. 30. (a) Difference in the force experienced by the tip at the steps for positive and negative bias, per unit applied volt [nN/V]. Open symbols correspond to steps on Al-Ni-Co quasicrystal surface. Filled symbols to steps on Au(111). The lines are calculations for 1 Debye and 0.45 Debye per step atom respectively; by definition they pass through the origin. The error bar is associated with the noise level of force measurement. (b) Electric field distribution calculated using the GICM in the tip-sample region with a permanent dipole close to the tip apex. (R=30 nm, D=0.5 nm).

The radii of the tips used for the Au and Al-Ni-Co samples derived from the force-distance curves was found to be 30 ± 11 nm, and 70 ± 30 nm respectively. Calculations performed for several values of tip radius and for 0.5 nm for D, are shown in figure 30(a) as a function of step height and step dipole moment (Park et al., 2005a). As we can see the data (difference in the force at + and – bias per unit applied volt) fit well the lines corresponding to step dipole values of 1.6 Debye/nm or 0.45 Debye/step atom for Au(111) monoatomic steps (Park et al., 2005a) with the tip radius of 30 nm, and 2.5 Debye/nm or 1.0 Debye/step atom for the smallest (0.2 nm) quasicrystal steps with the tip radius of 70 nm. We can conclude that the dipole moment scales proportionally to step height, at least for steps up to 1.5 nm.

The dipole moment obtained for Au(111) is ~3 times larger than the value of 0.16 Debye/atom obtained by Jia *et al.* (Jia et al., 1998a; 1998b) from STM barrier height measurements and ~2 times larger than the 0.20 to 0.27 Debye/atom obtained by Besocke *et al.* (Besocke & Wagner, 1973) from work-function measurements on stepped Au(111). Bartels *et al.* (Bartels et al., 2003) obtained 0.33 Debye/atom for Cu(111) steps from STM spectroscopy of localized states at step edges. Apart from systematic and statistical errors in the measurements, the discrepancy could be related to the very different methods used, tunneling barrier in one case and average work function in another as compared to direct measurement of the dipole force field in the present work.

6. Conclusions

In conclusion, we have studied the nanotribological behavior of a well-defined hydrogen-terminated diamond(111)/tungsten-carbide single asperity contact in UHV as a function of applied load. Local contact conductance measurements showed no significant changes in the shape of I-V curves for loads up to 1.7 μN, as expected from the proportionality between the current and the contact area, which provided us with a direct and independent way of measuring the area of contact. The DMT model provided an excellent fit to the current (contact area) versus load data for a variety of bias voltages, which is in agreement with the finding that $\mu = 0.02 < 0.1$. Using the DMT-relation for contact area versus load, we found that for this ideal single-asperity contact, *i.e.* one of the hardest, stiffest known heterocontacts, involving materials of great tribological importance, friction is directly proportional to the contact area: $F_f = \tau A$, where $\tau = 238$ MPa for loads up to 12 nN.

By using AFM and STM with the same conductive WC-coated cantilevers, we were able to study the tribological and electronic properties of nanocontacts and to correlate these properties with the degree of passivation of the interface. Contacts could be classified as clean, half-passivated and fully passivated, depending on whether none, one or both of the participating surfaces are covered with chemically inactive layers. While it would be desirable to obtain detailed information on the specific chemistry and structure of these contaminant species, no technique currently exists for obtaining such information at a confined nanoscale interface. Rather, we are restricted to rely on wide-scale AES measurements of the surfaces. Based on these measurements, we propose that the passivating materials for the WC tips consist mostly of strongly bound O and C species. On the tip they could be removed by sliding contact under high load on the Pt substrate. In the case of Pt, the contaminants were C species.

The clean Pt(111) surface could be imaged in STM mode with cantilevers stiff enough to avoid the jump-to-contact instability. When such a surface is brought into contact with a clean tip, strong bonds are formed that cause rupture of the contact in the bulk part of the tip and/or substrate upon separation. Sliding is strongly impeded in this case and always leads to severe cantilever deformations and distorted force-displacement curves.

With passivated tips, low adhesion energy contacts (~1 J/m^2) are formed. The friction properties of such contacts depend on whether additional adsorbate layers are also present on the Pt surface. Passivated areas of the surface give rise to low friction and sigmoid-type I-V characteristics, typical of poorly conductive or semiconducting materials. Clean Pt areas produce Ohmic contact characteristics.

Clean Pt can be imaged in contact mode with passivated tips and gives rise to atomic lattice stick-slip friction with the Pt(111) lattice periodicity. This is the first time that a chemically active metal surface has been imaged in UHV in AFM contact-mode, revealing stick-slip with atomic lattice periodicity, and indicates that the passivating layer on the WC tip is bound strongly enough to the tip that material is not transferred to the active Pt even in conditions where substantial energy dissipation takes place during friction.

The results indicate that even in ultrahigh vacuum conditions, transfer of low-conductivity, passivating material can easily occur in nano-scale contacts. This demonstrates that detailed studies of third-body processes at the nanoscale are accessible with this AFM-STM multifunctional approach. The presence of these species substantially effects friction and adhesion. These results are relevant to the understanding of transfer film formation and its influence on the structural evolution and tribology of interfaces, whose inelastic properties are only beginning to be probed and understood at the nanometer scale.

We presented the first results of the combination of PCM and AFM techniques, in which current images, obtained on contacts many nanometers in diameter produced by very high loads (up to 5 GPa), reveal the atomic scale periodicity of the substrate. This surprising observation indicates that, even after averaging over many contact points of atomic dimension, the lattice periodicity does not average out.

We also showed that PCM is capable of measuring variations in local conductivity with a lateral resolution that is similar to the corresponding AFM resolution. Moreover, the technique is capable of separating mechanical and electrical contributions to the measured current. We were able to determine that local conductivity variations arise from different sources, namely, moiré superstructure and the conductivity to the underlying substrate.

We favor point-contact current imaging of lattice resolution as an explanation for many of the STM images on graphite presented in the past, especially in the first decade of STM experiments. In these experiments, it is likely that the tip was in contact with the surface, as in PCM, which explains the weak dependence of "tunneling" current as a function of tip distance.

Point contact current imaging, in conjunction with simultaneous friction and topographic imaging, should be an important tool in current efforts to understand the atomic origin of friction. We are currently applying these techniques to study the tribological behavior of surfaces.

Finally, we have shown the existence of localized dipole fields in the vicinity of steps through direct measurements of the forces experienced by a biased STM tip. Together with measurements of the tip radius (from force-distance curves) and tip-sample distance (from current-distance approach curves) in the course of the same experiment, the method provides a direct way to map out and to measure local dipole moments on surfaces that should be of significance in studies of chemical and electronic properties of surfaces.

7. Acknowledgments

The work presented here was done at Materials Sciences Division, Lawrence Berkeley National Laboratory, Berkeley, CA 94720

Many thoughts, analyses, suggestions, and conclusions in this work were generated from research by and discussions with the following people: Dr. R.W. Carpick, Dr. D. F. Ogletree, Dr. J. Y. Park, Dr. R.J.A. van den Oetelaar, Dr. X. Lei, Mr. D. Schleef and Dr. M. Salmeron.

This work was supported by the Director, Office of Energy Research, Office of Basic Energy Sciences, Materials Sciences Division, of the U.S. Department of Energy under Contracts No. DE-AC03-76SF00098, DE-FG02-02ER46016, and DE-AC02-05CH11231. Also, this work was supported by the Ministry of Education, Research, Youth and Sport, Romania, and by the European Union through the European Regional Development Fund, and by Romanian National Authority for Scientific Research, under project POSCCE-O 2.1.2-2009-2/12689/717.

8. References

Arai, T. & Tomitori, M. (2000). Bias dependence of Si(111) 7x7 images observed by noncontact atomic force microscopy. *Appl. Surf. Sci.*, Vol. 157, pp. (207-211)

Atamny, F. & Baiker, A., (1995). Direct imaging of the tip shape by AFM. *Surf. Sci.*, Vol. 323, pp. (L314 –L318)

Barrena, E., Kopta, S., Ogletree, D.F., Charych, D.H., & Salmeron, M., (1999). Relationship between friction and molecular structure: Alkylsilane lubricant films under pressure. *Phys. Rev. Lett., Vol.* 82, pp. (2880-2883)

Bartels, L., Hla, S. W., Kühnle, A., Meyer G. & Rieder, K. H. & Manson, J. R. (2003). STM observations of a one-dimensional electronic edge state at steps on Cu(111). *Phys. Rev.B,* Vol. 67, No. 20, pp.(205416-205420)

Batra, I. P., Garcia, N., Rohrer, H., Salemink, H., Stoll, E. & Ciraci, S. (1987). A study of graphite surface with STM and electronic-structure calculations. *Surf. Sci.,* Vol. 181, pp. (126-138)

Batra I. P. & Ciraci, S. (1988). Theoretical scanning tunneling microscopy and atomic force microscopy study of graphite including tip surface interaction. *J. Vac. Sci. Technol.* A, Vol. 6, pp. (313-318)

Besocke, K. & Wagner, H. (1973). Adsorption of W on W(110): Work-Function Reduction and Island Formation. *Phys. Rev.B,* Vol. 8, pp. (4597-4600)

Besocke, K., Krahl-Urban B. & Wagner, H. (1977). Dipole moments associated with edge atoms; A comparative study on stepped Pt, Au and W surfaces. *Surf. Sci.,* Vol. 68, pp. (39-46)

Binnig, G., Rohrer, H., Gerber H., & Weibel E. (1983). 7x7 reconstruction on Si(111) resolved in real space. *Phys. Rev. Lett.*, Vol. 50, pp. (120-123)

Binnig, G., Quate, C.F. & Gerber, Ch. (1986). Atomic Force Microscope. *Phys. Rev. Lett.* Vol. 56, pp. (930- 933)

Binnig, G., Fuchs, H., Gerber, C., Rohrer, H., Stoll, E., & Tosatti, E. (1986). Energy-dependent state-density corrugation of a graphite surface as seen by scanning tunneling microscopy. *Europhys. Lett.*, Vol. 1, pp. (31-36)

Bennewitz, R., Gyalog, T., Guggisberg, M., Bammerlin, M., Meyer, E., & Güntherodt, H.J., (1999). Atomic-scale stick-slip processes on Cu(111). *Phys. Rev. B,* Vol. 60, pp. (R11301-R11304)

Bennewitz, R., Gnecco, E., Gyalog, T., & Meyer, E., (2001). Atomic friction studies on well-defined surfaces. *Trib. Lett.*, Vol. 10, pp.(51-56)

Dai, Q., Vollmer, R., Carpick, R.W., Ogletree, D.F., & Salmeron, M., (1995). Variable-temperature ultrahigh-vacuum atomic-force microscope . *Rev. Sci. Instrum.,* Vol. 66, pp. (5266-5271)

Daly, C., & Krim, J. (1996). Friction and damping of Xe/Ag(111). *Surf. Sci.*, Vol. 368, pp. (49-54)

Derjaguin , B. V., Muller, V. M., Toporov, Y. P., (1975). Effect of contact deformations on the adhesion of particles. *J. Colloid Interface Sci*., Vol. 53, pp. (314-326)

Dowson, D. (1998). *History of Tribology*, Longman, London

Enachescu, M., van den Oetelaar R.J.A., Carpick R.W., Ogletree D.F., Flipse C.F.J., & Salmeron M., (1998). Atomic force microscopy study of an ideally hard contact: The diamond(111)/tungsten carbide interface. *Phys. Rev. Lett.,* Vol. 81, pp. (1877-1880)

Enachescu, M., van den Oetelaar, R.J.A., Carpick, R.W., Ogletree, D.F., Flipse C.F.J., & Salmeron, M., (1999). Observation of proportionality between friction and contact area at the nanometer scale. *Trib. Lett.,* Vol. 7, pp. (73-78)

Enachescu, M., Schleef, D., Ogletree, D.F. & Salmeron, M.(1999). Integration of Point-Contact Microscopy and Atomic-Force Microscopy: Application to Characterization of Graphite/Pt(111). Phys. Rev. B, Vol. 60, pp. (16913-16919)

Enachescu, M., Carpick, R.W., Ogletree, D.F., & Salmeron, M.(1999). Making, breaking and sliding of nanometer-scale contacts. *Mat. Res. Soc. Symp. Proc.,* Vol. 539, pp. (93-103)

Enachescu, M., Carpick, R.W., Ogletree, D.F., & Salmeron, M.(2004). The role of contaminants in the variation of adhesion, friction, and electrical conduction properties of carbide-coated scanning probe tips and Pt(111) in ultrahigh vacuum. *J. App. Phys.,* Vol. 95, No. 12, pp. (7694-7700)

Carpick, R.W., Agraït, N., Ogletree, D.F., & Salmeron, M. (1996). Measurement of interfacial shear (friction) with an ultrahigh vacuum atomic force microscope, *J. Vac. Sci. Technol.* B, Vol.14, pp. (1289-1295)

Carpick, R. W., Agraït, N., Ogletree, D. F., & Salmeron, M., (1996). Variation of the interfacial shear strength and adhesion of a nanometer-sized contact. *Langmuir,* Vol. 12, pp. (3334-3340)

Carpick, R.W. & Salmeron, M., (1997). Scratching the surface: Fundamental investigations of tribology with atomic force microscopy . *Chem. Rev.* Vol. 97, pp. (1163-1194)

Carpick R.W., Enachescu M., Ogletree D.F., & Salmeron M., (1998). Making, Breaking and Sliding of Nanometer-Scale Contacts, *Proceedings of the MRS Fall Meeting,* Boston, October 1998

Carpick, R.W., Dai, Q., Ogletree, D.F., & Salmeron, M., (1998). Friction force microscopy investigations of potassium halide surfaces in ultrahigh vacuum: structure, friction and surface modification .*Tribol. Lett.*, Vol. 5, pp. (91-102)

Cottrell A.H., (1988). *Introduction to the Modern Theory of Metals*, Institute of Metals, ISBN 0-904357-97-X, London

Drummond, C., Alcantar, N., Israelachvili, J., Tenne, R., Golan, Y., (2001). Microtribology and friction-induced material transfer in WS2 nanoparticle additives. *Advanced Functional Materials,* Vol. 11, pp.(348-354)

Fisher, I. R., Kramer, M. J., Islam, Z., Ross, A. R., Kracher, A., Wiener, T., Sailer, M. J., Goldman, A. I., & Canfield, P. C. (1999). On the growth of decagonal Al-Ni-Co quasicrystals from the ternary melt.*Philos. Mag. B,* Vol. 79, pp. (425-434)

Gardos, M.N., (1994). *Emerging CVD Science and Technology*, In *Synthetic Diamond,* K.E. Spear and J.P. Dismukes, pp. (419- 425), Wiley, New York

Gómez-Moñivas, S., Froufe-Pérez, L.S., Caamaño A.J. & Sáenz, J.J. (2001). Electrostatic forces between sharp tips and metallic and dielectric samples. *Appl. Phys. Lett.,* Vol. 79, pp. (4048-4050)

Greenwood, J.A., & Williamson, J.B.P. (1966). *Proc. R. Soc. London*, *Ser. A,* Vol. 295, pp. (300-309)

Greenwood, J.A., (1997). *Proc. R. Soc. London*, *Ser. A* Vol. 453, pp. (301-306)

Greenwood, J. A. & Johnson, K. L. (1998). An alternative to the Maugis model of adhesion between elastic spheres. *J. Phys.* D, Vol. 31, pp. (3279-3290)

Grierson, D.S. & Carpick R.W. (2007). Nanotribology of Carbon-based Materials. *Nano Today*, Vol. 2, No. 5, pp. (12-21)

Guggisberg, M., Bammerlin, M., Baratof, A., Lüthi, R., Lopacher, Ch., Battison, F. M., Lü, J., Bennewitz, R., Meyer, E. & Güntherodt, H.-J. (2000). Dynamic force microscopy across steps on the Si(111)-(7 x 7) surface. *Surf. Sci.,* Vol. 461, pp. (255-265)

Harrison, J.A., & Brenner, D.W. (1995). *Handbook of Micro/Nanotribology*, CRC Press, ISBN-10: 084938401X, Boca Raton

Hansma, P. K. (1985). *Bull. Am. Phys. Soc.,* Vol. 30, pp. (251-254)

He, G., Muser, M. H., & Robbins, M. O., (1999). Adsorbed layers and the origin of static friction. *Science,* Vol. 284, pp. (1650-1652)

He, G. & Robbins, M. O., (2001). Simulations of the static friction due to adsorbed molecules. *Physical Review* B, Vol. 64, No. 3, pp. (035413-035425)

Homola, A.M., Israelachvili, J.N., Gee M.L., & McGuiggan P.M., (1989). Measurements of and relation between the adhesion and friction of 2 surfaces separated by molecularly thin liquid-films. *J. Tribol.* Vol. 111, pp. (675-682)

Hu, Z., Ogletree, D. F., Van Hove, M. A. & Somorjai, G. A. (1987). Leed theory for incommensurate overlayers - application to graphite on Pt(111). *Surf. Sci.,* Vol. 180, pp. (433-459)

Hu, J., Xiao, X.-D., Ogletree, D.F., & Salmeron, M., (1995). Atomic-scale friction and wear of mica. *Surf. Sci.*, Vol. 327, pp. (358-370)

Hurtado, J. & Kim, K.-S., (1998) Fracture and Ductile versus Brittle Behavior: Theory, Modeling, and Experiment, *Proceedings of the MRS Fall Meeting*, Boston, 1998

Ishida, H. & Liebsch, A. (1992). Calculation of the electronic-structure of stepped metal-surfaces. *Phys. Rev. B,* Vol. 46, pp. (7153-7156)

Israelachvili, J.N. & Tabor, D. (1972). The Measurement of Van Der Waals Dispersion Forces in the Range 1.5 to 130 nm. *Proc. Roy. Soc. A*, London, November 1972, Vol.331, No. 1584, pp. (19-38)

Israelachvili, J.N., McGuiggan, P.M., & Gee, M.L., (1990). Fundamental experimental studies in tribology - the transition from interfacial friction of undamaged molecularly smooth surfaces to normal friction with wear. *Wear*, Vol. 136, pp. (65-83)

Israelachvili, J. N.(1992). *Intermolecular and Surface Forces,* Academic Press London, London

Jackson, J. D. (1975). *Classical Electrodynamics*, John Wiley & Sons, ISBN 978-0-471-43132-9, New York

Jansen, A.G.M., van Gelder, A.P., & Wyder, P., (1980). Point-contact spectroscopy in metals. *J. Phys. C (Sol. State Phys.).* Vol.13, pp. (6073-6118)

Jia, J. F., Inoue, K. , Hasegawa, Y., Yang W. S. & Sakurai, T. (1998). Variation of the local work function at steps on metal surfaces studied with STM. *Phys. Rev. B,* Vol. 58, pp. (1193-1196);

Jia, J. F., Hasegawa, Y., Inoue, K., Yang, W. S. & Sakurai, T.(1998). Steps on the Au/Cu(111) surface studied by local work function measurement with STM. *Appl. Phys. A,* Vol. 66, pp. (S1125-S1128)

Johnson, K. L., Kendall, K., & Roberts, A. D., (1971). *Proc. Roy. Soc. London,* Vol. A 324, pp. (301-306)

Johnson, K.L., (1987). *Contact Mechanics*, Cambridge University Press, Cambridge

Johnson, K.L., (1996). Continuum mechanics modeling of adhesion and friction. *Langmuir* Vol.12, pp. (4510-4513)

Johnson, K.L., (1997). *Proc. R. Soc. London, Ser. A 453,* pp. (163-171)

Kishida, M., Kamimura, Y., Tamura, R., Edagawa, K., Takeuchi, S., Sato, T., Yokoyama, Y., Guo, J. Q. & Tsai, A. P. (2002). Scanning tunneling microscopy of an Al-Ni-Co decagonal quasicrystal. *Phys. Rev. B,* Vol. 65, No. 9, pp.(094208-094215)

Klein, C.A., (1992). Anisotropy of young modulus and poisson ratio in diamond. *Mater. Res. Bull.*, Vol. 27, pp. (1407-1414)

Kral-Urban, B., Niekisch, E. A & Wagner, H. (1977). Work function of stepped tungsten single crystal surfaces. *Surf. Sci.,* Vol. 64, pp. (52-68)

Krim, J., Watts, E.T. & Digel, J. (1990). Slippage of simple liquid-films adsorbed on silver and gold substrates. *J. Vac. Sci. Technol. A*, Vol. 8, pp. (3417-3420)

Krim, J., Solina, D.H., & Chiarello, R. (1991). Nanotribology of a Kr monolayer - a quartz-crystal microbalance study of atomic-scale friction. *Phys. Rev. Lett.,* Vol. 66, pp. (181-184)

Krim, J. (1996). Friction at the atomic scale. *Sci. Am.,* Vol. 275, pp. (74-80)

Kuwabara, M., Clarke, D. R. & Smith, D. A. (1990). Anomalous superperiodicity in scanning tunneling microscope images of graphite. *Appl. Phys. Lett.,* Vol. 56, pp. (2396-2398)

Land, T.A., Michely, T., Behm, R. J., Hemminger, J. C. & Comsa, G. (1992). STM investigation of single layer graphite structures produced on Pt(111) by hydrocarbon decomposition. *Surf. Sci.,* Vol. 264, pp. (261-270)

Land, T.A., Michely, T., Behm, R. J., Hemminger, J. C. & Comsa, G. (1992). Direct observation of surface-reactions by scanning tunneling microscopy - ethylene-]ethylidyne-]carbon particles-]graphite on pt(111). *J. Chem. Phys.*, Vol. 97, pp. (6774-6783)

Lantz, M.A., O'Shea, S.J., Welland, M.E., & Johnson, K.L. (1997). Atomic-force-microscope study of contact area and friction on NbSe2. *Phys. Rev. B,* Vol. 55, pp. (10776-10785);

Lantz, M.A., O'Shea, S.J., & Welland, M.E., (1997). Simultaneous force and conduction measurements in atomic force microscopy. *Phys. Rev. B,* Vol. 56, pp. (15345-15352)

Mamin, H. J., Ganz, E., Abraham, D. W., Thomson, R. E. & Clarke, J. (1986). Contamination-mediated deformation of graphite by the scanning tunneling microscope. *Phys. Rev.* B, Vol. 34, pp. (9015-9018)

Marchon, B., Ogletree, D. F. & Salmeron, M. (1988). Scanning tunneling microscopy study of the RE(0001) surface passivated by one-half a monolayer of sulfur in an atmospheric-environment. *J. Vac Sci. Tech. A,* Vol. 6, pp. (531-533)

Marti, O., Drake, B. & Hansma, P. K. (1987). Atomic force microscopy of liquid-covered surfaces - atomic resolution images. *Appl. Phys. Lett.,* Vol. 51, pp. (484-486)

Mate, C.M., McClelland, G.M., Erlandsson, R., & Chiang, S. (1987). Atomic-scale friction of a tungsten tip on a graphite surface. *Phys. Rev. Lett.* Vol. 59, pp. (1942- 1945)

Maugis D., (1992). Adhesion of spheres – The JKR-DMT transition using a Dugdale model. *J. Colloid Interface Sci.* Vol. 150, pp. (243-268)

McFadden, C.F. & Gellman, A., (1997). Metallic friction: the influence of atomic adsorbates at submonolayer coverages.*J., Surf. Sci.,* Vol. 391, pp. (287-299)

Mesa, G., Dobado-Fuentes E. & Sáenz, J. J. (1996). Image charge method for electrostatic calculations in field-emission diodes. *J. Appl. Phys.,* Vol. 79, pp.(39-44)

Müller, V.M., Yushenko, V.S., & Derjaguin, B.V., (1980). On the influence of molecular forces on the deformation of an elastic sphere and its sticking to a rigid plane. *J. Colloid Interface Sci.* Vol.77, pp. (91-101)

Müller, V.M., Derjaguin, B.V., & Toporov, Y.P., (1983). On 2 methods of calculation of the force of sticking of an elastic sphere to a rigid plane. *Colloids Surf.* Vol. 7, pp. (251-259)

Ogletree, D. F., Carpick, R. W., & Salmeron, M., (1996). Calibration of frictional forces in atomic force microscopy. *Rev. Sci. Instrum.,* Vol. 67, pp. (3298-3306)

Park, S.-I. & Quate, C. F. (1986). Tunneling microscopy of graphite in air. *Appl. Phys. Lett.*, Vol. 48, pp. (112-114)

Park, J. Y., Ogletree, D. F., Salmeron, M., Jenks C. J. & Thiel, P. A. (2004). Friction and adhesion properties of clean and oxidized Al-Ni-Co decagonal quasicrystals: a UHV atomic force microscopy/scanning tunneling microscopy study. *Tribol. Let.,* Vol. 17, pp. (629-636)

Park, J.Y., Sacha, G.M., Enachescu, M., Ogletree, D.F., Ribeiro, R.A., Canfield, P.C., Jenks, C.J., Thiel, P.A., Sáenz J.J., & Salmeron M. (2005). Sensing dipole fields at atomic steps with combined scanning tunneling and force microscopy. *Phys. Rev. Lett.,* Vol. 95, No. 13, 136802

(Park et al., 2005b) Park, J. Y., Ogletree, D. F., Salmeron, M., Ribeiro, R.A., Canfield, P.C., Jenks C. J. & Thiel, P. A.. (2005). Elastic and inelastic deformations of ethylene-passivated tenfold decagonal Al-Ni-Co quasicrystal surfaces. *Phys. Rev. B,* Vol. 71, No. 14, pp. (144203-144203-5);

Park, J. Y., Phaneuf, R.J., Ogletree, D.F., & Salmeron, M. (2005). Direct measurement of forces during scanning tunneling microscopy imaging of silicon pn junctions. *Appl. Phys. Lett*., Vol. 86, No. 17, A pp. (172105-172105-3)

Persson, B. N. J., & Volokitin, A. I. (1995). Electronic friction of physisorbed molecules. *J. Chem. Phys.,* Vol. 103, pp. (8679-8683).

Persson, B. N. J. & Nitzan, A.(1996). Linear sliding friction: on the origin of the microscopic friction for Xe on silver. *Surf. Sci.,* Vol. 367, pp. (261- 275)

Qian, L. M., Xiao, X. D., & Wen, S. Z., (2000). Tip in situ chemical modification and its effects on tribological measurements. *Langmuir,* Vol. 16, pp. (662-670)

Rubio, G., Agraït, N., & Vieira, S., (1996). Atomic-sized metallic contacts: Mechanical properties and electronic transport . *Phys. Rev. Lett.,* Vol. 76, pp. (2303 -2305)

Sacha, G. M. et al. (2005). Effective tip radius in electrostatic force microscopy. *Appl. Phys. Lett.*, Vol. 86, No. 12, pp.(123101-1 -123101-3)

Salmeron, M. , Ogletree, D. F., Ocal, C., Wang, H. C., Neubauer, G., Kolbe, W. & Meyers, G. (1991). Tip surface forces during imaging by scanning tunneling microscopy. *J. Vac. Sci. Technol.* B, Vol. 9, pp. (1347-1352)

Schwartz, M.M., (1990). *Ceramic Joining,* Materials Park, June 1990).

Seki, H., McClelland, G.M., & Bullock, D.C.(1987). Raman-spectroscopy of disk coatings in a working magnetic disk drive. *Wear* Vol. 116, pp. (381-391)

Selloni, A., Carnevali, P., Tosatti, E., & Chen, C. D. (1985). Voltage dependent Scanning Tunneling Microscopy of a crystal surface graphite. *Phys. Rev.* B. Vol. 31, pp. (2602-2605)

Selloni, A., Carnevali, P., Tosatti, E., & Chen, C. D. (1986). Correction. *Phys. Rev.* B, Vol. 34, pp. (7406-7406)

Shackelford, J.F., Alexander, W., & Park, J.S. (1994) *CRC Materials Science and Engineering Handbook*, CRC Press, Boca Raton

Sharvin, Y. V. (1965). *Sov. Phys.,* JETP, Vol. 21, pp. (655-658)

Sheiko, S.S., Möller, M., Reuvekamp, E.M.C.M., & Zandbergen, H.W., (1993). Calibration and evaluation of scanning-force-microscopy probes. *Phys. Rev.* B, Vol. 48, pp. (5675-5678)

Singer, I. L. (1992). *Fundamentals of Friction: Macroscopic and Microscopic Processes*, I. L. Singer & H. M. Pollock, Vol. 220, pp. (237-245), Kluwer, Dordrecht.

Singer, I. L., (1998). How third-body processes affect friction and wear. *MRS Bulletin,* Vol. 23, pp. (37-40)

Smith, D. P. E., Binnig, G., & Quate, C. F. (1986). Atomic point-contact imaging. *Appl. Phys. Lett.*, Vol. 49, pp. (1166-1168)

Smoluchowski, R. (1941). Anisotropy of the Electronic Work Function of Metals. *Phys. Rev.,* Vol. 60, pp. (661-674)

Sokoloff, J. B.(1993). Fundamental mechanisms for energy dissipation at small solid sliding surfaces. *Wear,* Vol. 167, pp. (59- 68)

Sokoloff, J. B. (1995). Theory of the contribution to sliding friction from electronic excitations in the microbalance experiment. *Phys. Rev. B,* Vol. 52, pp. (5318-5322)

Soler, J. M., Baro, A. M., Garcia, N. & Rohrer, H. (1986). Interatomic forces in scanning tunneling microscopy - giant corrugations of the graphite surface. *Phys. Rev. Lett.*, Vol. 57, pp. (444-447)

Sridhar, I., Johnson, K. L. & Fleck, N. A. (1997). Adhesion mechanics of the surface force apparatus. *J. Phys.* D, Vol. 30, pp. (1710-1719)

Stumpf, R. & Scheffler, M. (1996). Ab initio calculations of energies and self-diffusion on flat and stepped surfaces of Al and their implications on crystal growth. *Phys. Rev.B,* Vol. 53, pp. (4958-4973)

Sze, S.M., (1981). *Physics of Semiconductor Devices,* J. Wiley & Sons, New York

Szlufarska, I, Chandross, M., & Carpick R.W. (2008). Recent advances in single-asperity nanotribology. *J. Phys. D: Appl. Phys.,* Vol. 41, pp. (123001-1 - 123001-39)

Tabor, D. (1977). Surface forces and surface interactions. *J. Colloid Interface Sci.* Vol.58, pp. (2-13)

Tersoff, J. (1986). Anomalous corrugations in scanning tunneling microscopy - imaging of individual states. *Phys. Rev. Lett.*, Vol. 57, pp. (440-443)

Tsai, H. & Bogy, D.B., (1987). Characterization of diamond-like carbon-films and their application as overcoats on thin-film media for magnetic recording . *J. Vac. Sci. Technol.* A, Vol. 5, pp. (3287-3312)

van den Oetelaar, R.J.A. & Flipse, C.F.*J.,* (1997). Atomic-scale friction on diamond(111) studied by ultra-high vacuum atomic force microscopy. *Surf. Sci.,* Vol.384, pp. (L828-L835)

Yanson, I. K., Kulik, I. O. & Batrak, A. G. (1981). Point-contact spectroscopy of electron-phonon interaction in normal-metal single-crystals. *J. Low Temp. Phys*., Vol. 42, pp. (527-556)

Watts, E.T., Krim, J., & Widom, A. (1990). Experimental-observation of interfacial slippage at the boundary of molecularly thin-films with gold substrates. *Phys. Rev. B*, Vol. 41, pp. (3466-3472)

Wexler, G. (1966). *Proc. Phys. Soc. London,* Vol. 89, pp. (927-930)

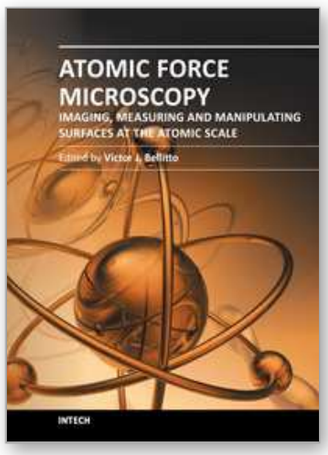

Atomic Force Microscopy - Imaging, Measuring and Manipulating Surfaces at the Atomic Scale

Edited by Dr. Victor Bellitto

ISBN 978-953-51-0414-8
Hard cover, 256 pages
Publisher InTech
Published online 23, March, 2012
Published in print edition March, 2012

With the advent of the atomic force microscope (AFM) came an extremely valuable analytical resource and technique useful for the qualitative and quantitative surface analysis with sub-nanometer resolution. In addition, samples studied with an AFM do not require any special pretreatments that may alter or damage the sample and permits a three dimensional investigation of the surface. This book presents a collection of current research from scientists throughout the world that employ atomic force microscopy in their investigations. The technique has become widely accepted and used in obtaining valuable data in a wide variety of fields. It is impressive to see how, in a short time period since its development in 1986, it has proliferated and found many uses throughout manufacturing, research and development.

InTech Europe
University Campus STeP Ri
Slavka Krautzeka 83/A
51000 Rijeka, Croatia
Phone: +385 (51) 770 447
Fax: +385 (51) 686 166
www.intechopen.com

InTech China
Unit 405, Office Block, Hotel Equatorial Shanghai
No.65, Yan An Road (West), Shanghai, 200040, China
中国上海市延安西路65号上海国际贵都大饭店办公楼405单元
Phone: +86-21-62489820
Fax: +86-21-62489821

IntechOpen